

Turbulence and skin friction modification in channel flow with streamwise-aligned superhydrophobic surface texture

T. O. Jelly, S. Y. Jung, and T. A. Zaki

Citation: *Physics of Fluids* (1994-present) **26**, 095102 (2014); doi: 10.1063/1.4894064

View online: <http://dx.doi.org/10.1063/1.4894064>

View Table of Contents: <http://scitation.aip.org/content/aip/journal/pof2/26/9?ver=pdfcov>

Published by the [AIP Publishing](#)

Articles you may be interested in

[Slip velocity of rigid fibers in turbulent channel flow](#)

Phys. Fluids **26**, 063302 (2014); 10.1063/1.4881942

[A numerical study of the effects of superhydrophobic surface on skin-friction drag in turbulent channel flow](#)

Phys. Fluids **25**, 110815 (2013); 10.1063/1.4819144

[Influence of an anisotropic slip-length boundary condition on turbulent channel flow](#)

Phys. Fluids **24**, 055111 (2012); 10.1063/1.4719780


[A theoretical prediction of friction drag reduction in turbulent flow by superhydrophobic surfaces](#)

Phys. Fluids **18**, 051703 (2006); 10.1063/1.2205307


[Effects of hydrophobic surface on skin-friction drag](#)

Phys. Fluids **16**, L55 (2004); 10.1063/1.1755723

A collection of five pieces of Pfeiffer Vacuum equipment. From top-left to bottom-right: a red rectangular turbopump, a cylindrical stainless steel backing pump, a white rectangular turbopump, a red cylindrical turbopump, and a large stainless steel chamber with a glass view window.

 Vacuum Solutions from a Single Source

- Turbopumps
- Backing pumps
- Leak detectors
- Measurement and analysis equipment
- Chambers and components

PFEIFFER  VACUUM

Turbulence and skin friction modification in channel flow with streamwise-aligned superhydrophobic surface texture

T. O. Jelly,¹ S. Y. Jung,¹ and T. A. Zaki^{1,2,a)}

¹Department of Mechanical Engineering, Imperial College, London SW7 2AZ, United Kingdom

²Department of Mechanical Engineering, Johns Hopkins University, Baltimore, Maryland 21218, USA

(Received 3 November 2013; accepted 8 August 2014; published online 5 September 2014)

Direct numerical simulations of turbulent flow in a channel with superhydrophobic surfaces (SHS) were performed, and the effects of the surface texture on the turbulence and skin-friction coefficient were examined. The SHS is modeled as a planar boundary comprised of spanwise-alternating regions of no-slip and free-slip boundary conditions. Relative to the reference no-slip channel flow at the same bulk Reynolds number, the overall mean skin-friction coefficient is reduced by 21.6%. A detailed analysis of the turbulence kinetic energy budget demonstrates a reduction in production over the no-slip phases, which is explained by aid of quadrant analysis of the Reynolds shear stresses and statistical analysis of the turbulence structures. The results demonstrate a significant reduction in the strength of streamwise vortical structures in the presence of the SHS texture and a decrease in the Reynolds shear-stress component (R_{12}) which has a favorable influence on drag over the no-slip phases. A secondary flow which is set up at the edges of the texture also effects a beneficial change in drag. Nonetheless, the skin-friction coefficient on the no-slip features is higher than the reference levels in a simple no-slip channel flow. The increase in the skin-friction coefficient is attributed to two factors. First, spanwise diffusion of the mean momentum from free-slip to no-slip regions increases the local skin-friction coefficient on the edges of the no-slip features. Second, the drag-reducing capacity of the SHS is further reduced due to additional Reynolds stresses, (R_{13}). © 2014 AIP Publishing LLC. [<http://dx.doi.org/10.1063/1.4894064>]

I. INTRODUCTION

Naturally occurring materials often possess properties which are of considerable fundamental and practical interest. For example, the leaves of several varieties of plant-life have superhydrophobic characteristics. A superhydrophobic state is attained naturally or synthetically through the combination of hydrophobic surface chemistry and small-scale surface features.¹ As water droplets come into contact with these surfaces, they tend to exhibit a beading behavior where, instead of spreading out, the droplets take the form of near-perfect spheres. As a consequence of the increased sphericity, the wetted area can be extremely small. In the presence of bulk fluid motion, hydrophobicity can lead to significant skin friction savings. The present study examines the mechanics of skin friction and turbulence modification in fully developed turbulent channel flow over SHS textures.

A. Experimental studies of SHS textures

Prior to the manufacture of patterned SHS textures, Watanabe *et al.*² studied the drag-reducing performance of circular pipes rendered water-repellent by the application of a porous hydrophobic

^{a)} Author to whom correspondence should be addressed.

silica agent. The Reynolds numbers based on the diameter spanned the range $100 < Re_D < 10\,000$. Watanabe *et al.*² reported a maximum laminar drag reduction of 14%, relative to the hydrophilic no-slip pipe and, beyond transition to turbulence, observed no drag reduction. They demonstrated that, for a fixed streamwise pressure gradient, the laminar bulk velocity increased due to a finite slip velocity at the wall. They also hypothesized that the liquid-gas interfaces supported in the microcracks played a central role in both the mechanisms of fluid slip and laminar drag reduction.

Ou *et al.*³ were among the first to experimentally demonstrate the suppression of skin friction in a laminar channel flow using patterned SHS textures. They conducted a series of experiments designed to investigate the effect that the texture width (20–30 μm) and spacing (15–150 μm) and channel height have on the levels of skin friction reduction. It was demonstrated that, for a fixed feature width, the laminar skin friction decreased with increasing feature spacing. In addition, for a fixed feature spacing, micro-posts consistently outperformed micro-ridges. A maximum drag reduction of 40% relative to no-slip microchannel was reported. All of the SHS textures studied by Ou *et al.*³ were found to operate in the Cassie-Baxter state.⁴ Beyond a critical feature spacing, however, SHS textures operate in a Wenzel state.⁵ In a subsequent study, Ou and Rothstein⁶ used micro-particle image velocimetry (μ -PIV) to examine the laminar flow of water past streamwise-aligned micro-ridges. Their measurements showed that wider feature spacing results in higher streamwise slip and, in turn, lower laminar drag. An alternative use of SHS textures in laminar flows is to enhance mixing while operating in the Cassie-Baxter state.⁷ For example, when micro-ridge textures are aligned at an oblique angle to the primary flow direction, a helical secondary flow is established which enhances mixing appreciably in comparison to a conventional no-slip surface.⁷

In the turbulent regime, experimental studies have also demonstrated the drag-reducing capabilities of SHS textures. Daniello *et al.*⁸ assessed the performance of two micro-ridge geometries (30 μm and 60 μm wide) over a range of Reynolds numbers $2000 < Re < 9500$. They reported inappreciable deviation from the no-slip channel below $Re = 4000$. Beyond this Reynolds number, however, significant turbulent drag reductions were reported with a maximum of 50%. Since turbulent drag reduction set in once the viscous sublayer thickness was similar in size to the texture spacing, Daniello *et al.*⁸ interpreted their results in terms of a critical Reynolds number.

Woolford *et al.*⁹ used μ -PIV to acquire measurements over a range of Reynolds numbers $4800 < Re < 10\,000$ for both longitudinally and transversely aligned micro-ridge SHS textures. SHS textures aligned parallel to the primary flow direction weakened the turbulence activity, and drag was reduced by approximately 11%. On the other hand, SHS textures aligned transversely to the primary flow direction enhanced the turbulence activity and increased drag by approximately 6.5%. Due to resolution limits of their μ -PIV apparatus, the measurement position closest to the wall was approximately 10 wall units. Consequently, the details of near-wall turbulence dynamics and quantification of any mean slip velocities were not possible.

The difficulties in experimentally obtaining near-wall measurements in turbulent flows motivated the use of direct numerical simulations (DNS) where fully resolved, time-dependent three-dimensional flow fields can be acquired. However, a suitable surface model of a SHS texture is required to study their effects. Two widely adopted surface models are discussed below along with previous numerical simulations of flows over SHS.

B. Theoretical and numerical studies of SHS textures

Theoretical and numerical studies of SHS textures require an appropriate surface model for the boundary conditions. To date, two separate surface models have been widely adopted in the literature. The first is referred to as the Navier slip model,¹⁰

$$u_s = l_u \left. \frac{\partial u}{\partial y} \right|_{y=0}, \quad w_s = l_w \left. \frac{\partial w}{\partial y} \right|_{y=0}, \quad (1)$$

where (u_s, w_s) are the slip velocities and (l_u, l_w) are the effective slip-lengths which can be prescribed isotropically, $l_u = l_w$, or anisotropically, $l_u \neq l_w$. This model has been widely adopted for simulations of internal^{11–13} and external¹⁴ flows.

Min and Kim¹² examined the stability of channel flow and transition to turbulence when the SHS texture was modeled using the Navier slip boundary condition. They concluded that exclusive streamwise slip was most effective in delaying transition to turbulence, whereas spanwise slip promoted it. In a similar study, Min and Kim¹¹ used DNS to investigate the effect of a hydrophobic surface on the levels of turbulent skin friction. In general, turbulent drag was reduced in the presence of streamwise slip, whereas it increased in the presence of spanwise slip. The theoretical predictions by Fukagata *et al.*¹⁵ also support the beneficial effects of streamwise slip and the detrimental effects of spanwise slip on turbulent drag over SHS. Busse and Sandham¹³ studied the effects of an anisotropic Navier slip-length boundary conditions on turbulent channel flow by systematically varying (l_u, l_w) and, depending on the relative magnitudes, they were able to effect drag reduction or increase relative to the reference flow. The same work showed that the organization of near-wall vortical structures is more regular in response to streamwise slip and is disrupted by spanwise slip.

The second SHS model was devised by Philip,^{16,17} and enforces regions of no-slip and free-slip boundary conditions to represent the micro-features and liquid-gas interfaces, respectively. In addition, the free-slip surfaces are assumed to be flat such that the modeled SHS appears planar with patterned boundary conditions. Philip¹⁶ derived analytical solutions for Stokes flow over a flat plate with longitudinal or transverse free-slip slots. This model was later extended by Lauga and Stone¹⁸ to analyze Stokes flow through a pipe with transverse free-slip stripes and, more recently, by Davis and Lauga¹⁹ to study flow past circular micro-post topologies. Starting from the mixed no-slip and free-slip boundary conditions, Ybert *et al.*²⁰ derived scaling laws to characterize the performance of numerous SHS and also examined the effects of interface curvature. In a later study, Cheng *et al.*²¹ simulated laminar flow over a range of Reynolds numbers, $1 < Re < 1000$, using the same mixed boundary conditions and evaluated various SHS textures. They noted that SHS performance exhibited a Reynolds number dependence except for streamwise-aligned ridges.

Martell *et al.*²² used DNS to study fully developed turbulent channel flow at a friction Reynolds number $Re_\tau \approx 180$ over SHS textures modeled using the mixed no-slip and free-shear boundary conditions. In total, Martell *et al.*²² considered seven unique surface topologies and reported the mean streamwise velocity profiles, slip velocities, Reynolds stress profiles, and wall shear stress levels. In a subsequent study by Martell *et al.*,²³ three friction Reynolds numbers $Re_\tau = \{180, 395, 590\}$ were considered and 14 different surface topologies were investigated. For the largest micro-feature spacing, an average slip velocity over 80% of the bulk velocity was reported, with a corresponding shear stress reduction of over 50%. In general, the results by Martell *et al.*^{22,23} demonstrated that drag reduction increases with increasing feature spacing. For a given feature width and feature spacing, micro-posts always outperformed micro-ridges and the performance increase was credited to an increased average streamwise slip velocity which in turn reduced the levels of the average wall shear stress.

In a recent study, Park *et al.*²⁴ used DNS to examine the response of laminar and turbulent channel flow to the presence of streamwise-aligned SHS micro-ridges. In laminar flows, the drag reduction was independent of Reynolds number and depended only on the surface geometry. In turbulent flow, however, a Reynolds number dependence is established. The authors explained performance trends in terms of the effective slip length in wall units.

C. Motivation and objectives

Despite several numerical^{22–24} and experimental^{8,9} studies, many characteristics of turbulence near SHS textures have not been examined. For example, an in-depth analysis of changes to the turbulence kinetic energy (TKE) budget near particular phases of the surface textures is not available. Previous studies often characterized SHS performance using streamwise and spanwise averaged quantities when phase-dependent data can be more instructive. Furthermore, changes in turbulent structures, e.g., near-wall streaks and vortices and their statistical properties, also remain unclear.

The present study examines in detail the factors that dictate the performance of streamwise-aligned SHS textures in fully turbulent channel flow. Recent experimental^{8,9} and computational^{22–24} studies have quantified the drag-reducing capacity of numerous surface topologies over a range of flow conditions in order to identify performance trends. The current study focuses on a single SHS

texture topology, namely, streamwise-aligned ridges. For this particular texture, Daniello *et al.*⁸ noted a close agreement in the wall shear stress reduction predicted by their experiments and the DNS by Martell *et al.*²² at the same Reynolds number.

This paper is organized into seven sections. Section II includes the numerical method, details of the superhydrophobic boundary conditions, phase-averaging procedures, a validation of the current DNS algorithm, and a grid independence study. Section III details the effect of the SHS texture on the mean flow; primary, secondary, and slipping fluid motions are presented. Section IV details the statistical response of the stochastic, or turbulent, fluid motions to the presence of the SHS texture. Section V focuses on the contributions of the primary, secondary, and stochastic fluid motions to the local levels of skin friction. Section VI investigates changes in the turbulence structures in the vicinity of the SHS. Finally, a summary of the present study is presented in Sec. VII.

II. COMPUTATIONAL ASPECTS

In the present study, direct numerical simulations of fully developed turbulent channel flow are performed at constant mass flow rate. The continuity and Navier-Stokes equations for an incompressible fluid are

$$\frac{\partial u_i}{\partial x_i} = 0, \quad (2a)$$

$$\frac{\partial u_i}{\partial t} + u_j \frac{\partial u_i}{\partial x_j} = -\frac{\partial p}{\partial x_i} + \frac{1}{Re_b} \frac{\partial^2 u_i}{\partial x_j \partial x_j}. \quad (2b)$$

The velocity components in the streamwise (x), wall-normal (y), and spanwise (z) directions are u , v , and w , respectively, and p is the pressure. The bulk Reynolds number in the momentum equations (2b), is defined as $Re_b \equiv U_b \delta / \nu$, where $U_b = \frac{1}{2\delta} \int_0^{2\delta} u dy$ is the bulk velocity, δ is the channel half-height, and ν is the kinematic viscosity. Since the mass flow rate is constant throughout the simulations, the bulk Reynolds number, Re_b , remains fixed. The friction Reynolds number is defined as $Re_\tau \equiv u_\tau \delta / \nu$, where the friction velocity is given by $u_\tau \equiv (\tau_w / \rho)^{1/2}$, and τ_w is the average shear stress at the wall and ρ is the density. Throughout this document the friction velocity of the reference no-slip channel is denoted $u_{\tau,0}$. Quantities non-dimensionalized by wall variables are marked by superscript $+$, e.g., $y^+ = yu_\tau / \nu$.

The Navier-Stokes equations are solved using a second-order accurate fractional step algorithm on a staggered grid with a local volume-flux formulation.²⁵ The diffusive terms are integrated in time implicitly using the Crank-Nicolson scheme and the nonlinear convective terms are treated explicitly using the Adams-Bashforth scheme. The pressure is discretized by an implicit Euler scheme. Periodic boundary conditions are enforced in both the streamwise and spanwise directions.

The computational domain, shown in Figure 1, is a rectangular volume ($L_x \times L_y \times L_z$) and is discretized using a Cartesian mesh with $N_x \times N_y \times N_z$ grid-points. A Cartesian grid conforms to the topology of SHS textures under consideration. Grid spacing is uniform in the streamwise and spanwise directions. In the wall-normal direction, a hyperbolic tangent stretching function is employed to cluster points near the bottom ($y/\delta = 0$) and top ($y/\delta = 2$) walls.

On both the bottom and top walls, the SHS texture is prescribed using mixed no-slip and free-slip boundary conditions. The SHS textures are comprised of streamwise-aligned micro-ridges of width

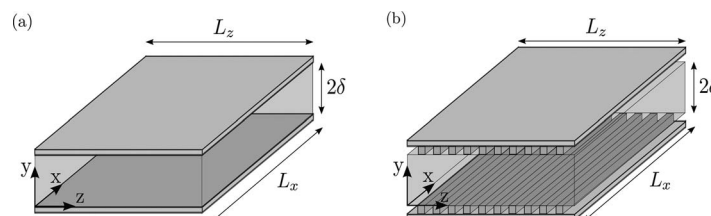


FIG. 1. Schematic of computational domain. (a) Reference no-slip channel flow; (b) SHS channel configuration.

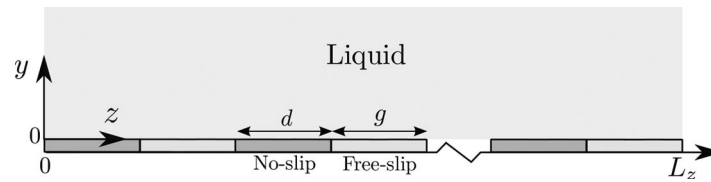


FIG. 2. Schematic of streamwise-aligned micro-ridge SHS texture. The no-slip and free-slip boundary conditions are enforced to model the micro-ridges and interfaces, respectively.

d , with a liquid-gas interface of width g supported between neighboring micro-ridges (Figure 2). The micro-ridges are modeled by enforcing the no-slip boundary conditions,

$$u = 0, v = 0, w = 0, \quad (3)$$

and the interfaces are modeled using the no-penetration and shear-free boundary conditions

$$\frac{\partial u}{\partial y} = 0, \quad v = 0, \quad \frac{\partial w}{\partial y} = 0. \quad (4)$$

In addition, the free-slip surface is modeled to be perfectly flat.

The spanwise repetition of the SHS texture motivates the definition of a spanwise phase,

$$\phi_z \equiv 2\pi \left(\frac{z}{d+g} \bmod 1 \right). \quad (5)$$

In the current flow configuration, it is desirable to isolate contributions from the periodic and stochastic motions. Therefore, the spatial analogue of the temporal phase-averaging procedures outlined by Hussain and Reynolds²⁶ is adopted,

$$\begin{aligned} a(\mathbf{x}, t) &= \underbrace{\langle A \rangle^{xz}}_{\langle a \rangle} + \tilde{a} + a'(\mathbf{x}, t) \\ &= \langle a \rangle + a'(\mathbf{x}, t), \end{aligned} \quad (6)$$

where a is the instantaneous variable, $\langle \cdot \rangle$ is the phase average, and a' is the stochastic component. For streamwise aligned ridges, $\langle a \rangle$ includes the time and streamwise averaging, $\langle a \rangle = \langle a \rangle^x$. Note that the spatial mean can be written as

$$\langle A \rangle^{xz} = \frac{1}{2} (\langle A \rangle^{\text{ns}} + \langle A \rangle^{\text{fs}}), \quad (7)$$

where superscripts “ns” and “fs” denote averages over all no-slip and free-slip phases, respectively. For example, the instantaneous velocity can be decomposed according to

$$\begin{aligned} u_i(\mathbf{x}, t) &= \frac{1}{2} (\langle U_i(y) \rangle^{\text{ns}} + \langle U_i(y) \rangle^{\text{fs}}) + \tilde{u}_i(y, z) + u'_i(\mathbf{x}, t) \\ &= \langle U_i(y) \rangle^{xz} + \tilde{u}_i(y, z) + u'_i(\mathbf{x}, t). \end{aligned} \quad (8)$$

In the mean-flow equations,

$$\frac{\partial \langle u_i \rangle}{\partial t} + \langle u_j \rangle \frac{\partial \langle u_i \rangle}{\partial x_j} = -\frac{\partial \langle p \rangle}{\partial x_i} + \frac{1}{Re_b} \frac{\partial^2 \langle u_i \rangle}{\partial x_j \partial x_j} - \frac{\partial \langle R_{ij} \rangle}{\partial x_j}, \quad (9)$$

the phase-averaged Reynolds stresses are

$$\begin{aligned} \langle R_{ij} \rangle &= \langle u'_i u'_j \rangle \\ &= \langle (u_i - \langle u_i \rangle)(u_j - \langle u_j \rangle) \rangle. \end{aligned} \quad (10)$$

A. Validation

In order to verify the accuracy and reliability of the current DNS algorithm, results from the work by Kim *et al.*²⁷ were reproduced. The discretization details from that work and the current

TABLE I. Discretization details in the work by Kim *et al.*²⁷ and by Martell *et al.*²² and their respective validation cases, V1 and V2. All wall units are evaluated using the friction velocity from the reference no-slip channel flow, $u_{\tau,0}$.

Case	L_x/δ	L_z/δ	Δx^+	Δz^+	Δy_{\max}^+	y_{\min}^+
Kim <i>et al.</i> ²⁷	4π	3π	11.78	7.07	4.40	0.05
V1	4π	3π	5.89	3.53	4.04	0.17
Martell <i>et al.</i> ²²	6	3	8.44	4.22
V2	6	3	8.44	4.22	4.04	0.17

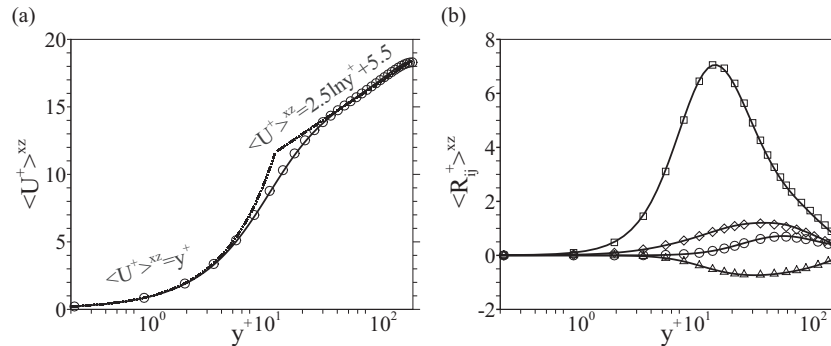


FIG. 3. Validation against results by Kim *et al.*²⁷ (a) Mean streamwise velocity profile; (b) Reynolds stresses. Results by Kim *et al.*²⁷ are plotted as symbols. All quantities are normalized using $u_{\tau,0}$.

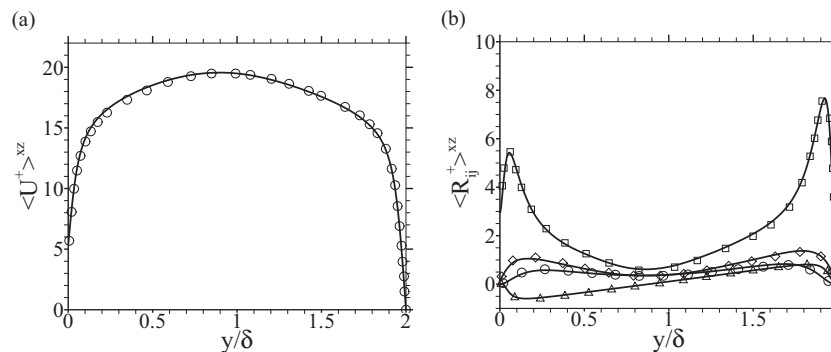


FIG. 4. Validation against results by Martell *et al.*²² (a) Mean streamwise velocity profile; (b) Reynolds stresses. Results by Martell *et al.*²² are plotted as symbols. All quantities are normalized using $u_{\tau,0}$.

simulation (case V1) are reported in Table I. Figure 3 compares the mean streamwise velocity profiles and Reynolds stress profiles, and an excellent level of agreement is observed.

In order to verify the accuracy and reliability of the current DNS algorithm in simulating turbulent channel flow over SHS textures, the results corresponding to the “30–30 μm ” ridges case by Martell *et al.*²² were reproduced. Similar to their computational setup, the simulation was performed at a constant mean streamwise pressure gradient, corresponding to the friction Reynolds number $Re_{\tau} \approx 180$. The SHS texture was only prescribed on the bottom wall and has non-dimensional feature width and spacing of $(d + g)^+ = 67.5$ repeated eight times in the spanwise direction. Figure 4 compares the mean streamwise velocity profiles and Reynolds stress profiles from the current data (case V2 in Table I) and the study by Martell *et al.*²² Here too an excellent level of agreement is observed.

B. Flow parameters and simulation setup

There are two principal differences between the hereafter adopted computational setup and that by Martell *et al.*²² First, those authors prescribed SHS textures on the bottom wall only which leads

TABLE II. Grid independence study. Grid A matches the resolution adopted by Martell *et al.*^{22,23} and by Park *et al.*²⁴ Grid F is adopted throughout the remainder of this work. Note that percent errors are computed relative to grid B. For all grids, $(L_y, L_z)/\delta = (2, 3)$. All wall units are evaluated using $u_{\tau,0}$.

Grid	L_x/δ	N_x	N_y	N_z	Δx^+	Δy_{\min}^+	Δy_{\max}^+	Δz^+	$\langle C_f \rangle^{xz}$ ($\times 10^3$)	Error (%)	$\langle U_s \rangle^{xz}$	
A	6	128	128	128	8.44	0.19	7.22	4.22	5.88	4.85	0.29	Refs. 22–24
B	6	128	128	512	8.44	0.19	7.22	1.06	6.18	...	0.27	...
C	6	256	128	512	4.22	0.19	7.22	1.06	6.21	0.49	0.27	<i>x</i> -refinement
D	6	128	256	512	8.44	0.09	3.62	1.06	6.16	0.32	0.27	<i>y</i> -refinement
E	6	128	128	1024	8.44	0.19	7.22	0.53	6.23	0.81	0.27	<i>z</i> -refinement
F	12	512	128	1024	4.22	0.19	7.22	0.53	6.35	...	0.27	Current grid

to an asymmetric flow about the channel half-height. In the current work, we prescribe SHS textures on both the top and bottom wall. This choice facilitates the derivation of a mathematical identity that describes the various dynamical contributions to skin friction (Sec. V). Second, Martell *et al.*²² chose to hold the streamwise pressure gradient constant, corresponding to a friction Reynolds number of $Re_\tau = 180$, and the influence of the texture, therefore, is to increase the bulk velocity, U_b . In the current work, we hold the mass flow rate constant, and hence changes in drag can be inferred from monitoring the mean streamwise pressure gradient or the skin-friction coefficient. The choice of constant mass flow rate has been widely adopted in studies of flow control including, for example, spanwise wall oscillations,²⁸ riblets,²⁹ active blowing and suction,³⁰ and SHS textures.¹¹

The grid resolution and the size of the computational domain are compared to previous studies^{22–24} in Table II. Given the spanwise change in the boundary condition at the texture surface, an extensive spanwise grid refinement study was performed. Three different spanwise grids are reported in Table II. Relative to grid A which has a resolution commensurate with recent studies,^{22–24} the mean skin friction and streamwise slip vary by 5% and 7% upon spanwise grid refinement by a factor of four (grid B). Further doubling the spanwise resolution (grid E) does not yield an appreciable change (less than 1%) in the mean skin-friction coefficient or streamwise slip velocity.

The phase-averaged skin-friction coefficients, $\langle C_f \rangle$, corresponding to grids B and E are compared in Figure 5(a). Doubling the spanwise resolution has little effect on the distribution of $\langle C_f \rangle$. The streamwise slip velocity profiles, $\langle U_s \rangle$, corresponding to grids B and E are compared in Figure 5(b) with similar conclusion. The current results therefore indicate that the SHS features are sufficiently resolved with $N_z = 512$ for the current flow conditions. The data in Table II also indicate that insufficient grid resolution in the spanwise direction results in an underestimation of the skin friction, as observed by Launder and Li.³¹ Further grid refinement checks were performed in both the streamwise and wall-normal directions (Table II). Relative to grid B, the number of grid points was doubled in each direction independently in grids C and D, and the change in the mean skin-friction coefficient was less than 0.5%.

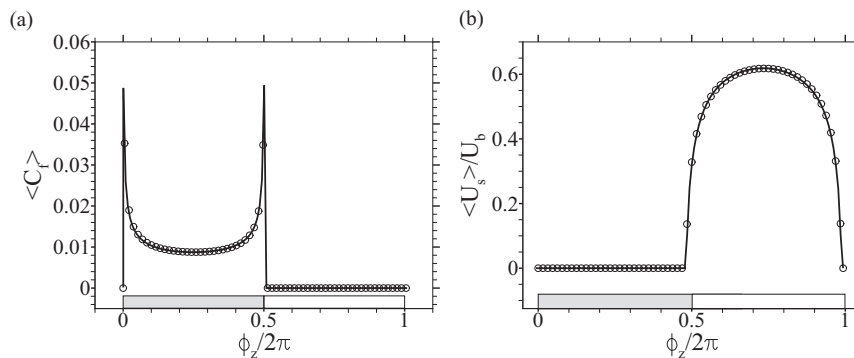


FIG. 5. Comparison of phase-averaged statistics obtained on grid B (○) and grid E (—). (a) Skin-friction coefficient, $\langle C_f \rangle$; (b) streamwise slip velocity, $\langle U_s \rangle$.

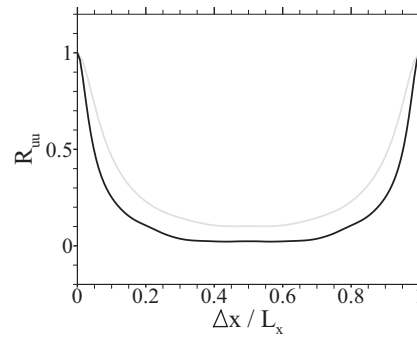


FIG. 6. Streamwise two-point correlation, R_{uu} , at $y^+ = 10.4$ for SHS case. (Grid B: —) $L_x = 6$ and (Grid F: - - -) $L_x = 12$.

Since the surface texture is aligned in the streamwise direction, it is important to examine the influence of the streamwise extent of the computational domain on the results. The two-point correlation,

$$R_{uu}(\Delta x) = \frac{\langle u'(x)u'(x + \Delta x) \rangle}{\langle u'u' \rangle}, \quad (11)$$

was evaluated for two domain lengths, $L_x/\delta = 6$ (grid B) and $L_x/\delta = 12$ (grid F). Figure 6 shows the results at the wall-normal position $y^+ = 10.4$. The correlation decays to $R_{uu} = 0.11$ for the short domain and to $R_{uu} = 0.02$ for the longer L_x . We have therefore adopted the longer extent, $L_x/\delta = 12$, which is twice the domain length used in earlier studies.^{22–24}

All the results presented herein correspond to grid F (see Table II). Therefore, 128 grid points are used in the span to resolve every SHS texture, where the no-slip micro-feature and free-slip interface are represented by 64 grid points each. The spanwise grid resolution used throughout this study is eight times finer than recent studies of the same flow configuration.^{22–24} In addition, a reference case with no-slip boundary conditions on both the top and bottom walls was simulated. The reference case was simulated on grid F using identical flow conditions, and at a bulk Reynolds number $Re_b = 2800$. For the reference case, the skin-friction coefficient agreed to within 1% of the value reported by Kim *et al.*²⁷

III. MEAN FLOW STATISTICS

This section presents the results for the mean fluid motion which is divided into three categories. First, the primary flow is reported, which is simply the fluid motion aligned with the primary (streamwise) flow direction. Second, the secondary flow is discussed, which is the periodic fluid motion in the cross-flow plane. Finally, the slip flow is examined.

A. Skin friction and primary flow

For a fully developed channel flow at constant mass flow rate, the mean streamwise pressure gradient is balanced by viscous losses. Figure 7 shows the spanwise distribution of skin friction across the SHS texture. Relative to the reference no-slip channel flow, the skin friction on the SHS texture is higher for all no-slip phases. By definition (Eq. (4)), skin friction is zero across all the free-slip phases.

The percentage change in the skin-friction coefficient averaged across all phases was computed,

$$DR = \left(\frac{\langle C_f \rangle^{xz} - \langle C_f \rangle_0^{xz}}{\langle C_f \rangle_0^{xz}} \right) \times 100, \quad (12)$$

where subscript 0 refers to the reference no-slip channel flow. Upon evaluation of Eq. (12), the percentage change in skin friction for the current SHS texture is $DR = -21.6\%$.

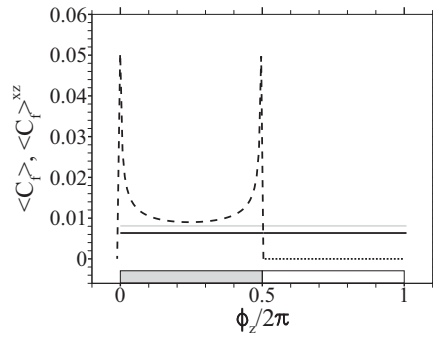


FIG. 7. Phase-averaged skin-friction coefficient, $\langle C_f \rangle$, at no-slip (---) and free-slip (····) phases. Also shown is the mean value across all phases $\langle C_f \rangle^{xz}$ (—), and the reference value for no-slip channel flow, $\langle C_f \rangle_0^{xz}$ (—).

Previous studies of fully developed turbulent channel flow over SHS have reported statistical quantities averaged in both the streamwise and spanwise directions, using both the Navier slip model^{11,13,15} and mixed no-slip/free-slip boundary conditions.^{22–24} Mean streamwise velocity profiles corresponding to the reference no-slip channel flow and the SHS case are shown in Figure 8(a), where each profile has been normalized by its respective friction velocity, u_τ . Compared to the reference case, the velocity profile above the SHS texture shows a shift of the viscous sublayer due to the mean streamwise slip velocity, $\langle U_s^+ \rangle^{xz}$, and an elevation of the log-law region. The latter observation is a common feature of drag reduction in turbulent flows and has been noted in connection with a broad range of passive^{29,32,33} and active^{11,28,30} flow control strategies. The mean profile normalized by the bulk velocity, U_b , is shown in Figure 8(b). Relative to the reference channel flow, the profile exhibits a streamwise momentum surplus (deficit) below (above) $y/\delta \approx 0.19$. Note that for the current configuration, $\langle V \rangle^{xz} = \langle W \rangle^{xz} = 0$.

In order to examine the cause of the spanwise variation in skin friction (see Figure 7), we analyze the primary flow using phase-averaged statistics. At the coarsest level, we decompose the mean streamwise velocity,

$$\langle U \rangle^{xz} = \frac{1}{2} (\langle U \rangle^{ns} + \langle U \rangle^{fs}). \tag{13}$$

Figure 9(a) shows the average velocity profiles for the no-slip phases, $\langle U^+ \rangle^{ns}$, normalized by the average friction velocity across the same area, u_τ^{ns} . Compared to the reference channel flow, the profile above the SHS collapses in the viscous sublayer, whereas a downward shift is observed in the log-law region. The latter observation is in contrast to the upward shift in $\langle U^+ \rangle^{xz}$ shown in Figure 8(a). The downward shift of $\langle U^+ \rangle^{ns}$ in the log-law region is consistent with the increase in the average skin friction across no-slip phases (Figure 7).

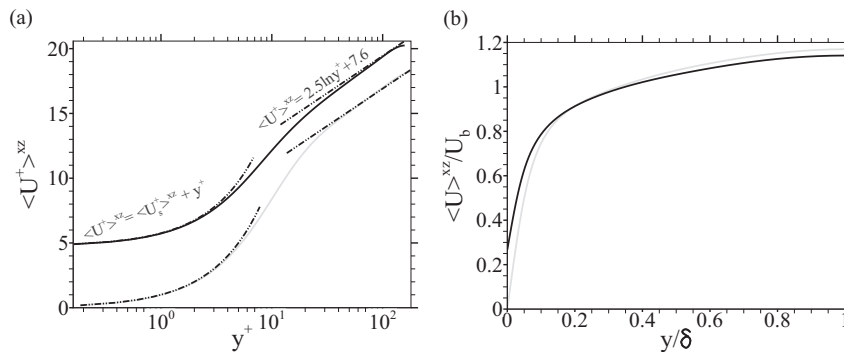


FIG. 8. Mean streamwise velocity profiles averaged across all phases and normalized by (a) the friction velocity u_τ and (b) the bulk velocity, U_b , for the SHS (—) and the reference no-slip channel flow (---).

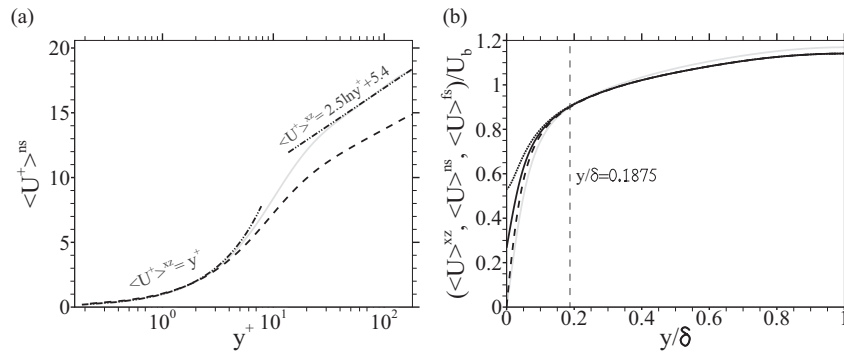


FIG. 9. Mean streamwise velocity profile averaged across all no-slip phases $\langle U^+ \rangle^{ns}$ (---) and all free-slip phases $\langle U^+ \rangle^{fs}$ (····). Profiles are normalized by (a) the friction velocity averaged across all no-slip phases, u_τ^{ns} , and (b) the bulk velocity, U_b . In both figures, the profile corresponding to the reference channel flow is also shown (—).

Figure 9(b) shows the decomposition of the mean streamwise velocity profile across all no-slip and free-slip phases (see Eq. (13)), where the profiles are normalized by the bulk velocity, U_b . A phase-dependence is observed below $y/\delta \approx 0.1875$; this wall-normal distance is equal to the spanwise width of the no-slip and the free-slip features. This observation is in agreement with the previous study by Martell *et al.*²³ who remarked that textured surfaces affect the near-wall region up to a distance less than or equal to the feature spacing.

To characterize the phase-dependence of the primary flow in more detail, contours of $\langle u \rangle$ are plotted on the transverse ϕ_z - y plane in Figure 10(a) for both the reference no-slip channel flow and the SHS case. Above the SHS texture, at $y/\delta \approx 0.1875$, the contours of streamwise velocity show weak phase-dependence which agrees well with the profiles shown in Figure 9(b). However, as the SHS texture is approached the contours become corrugated in the spanwise direction. The

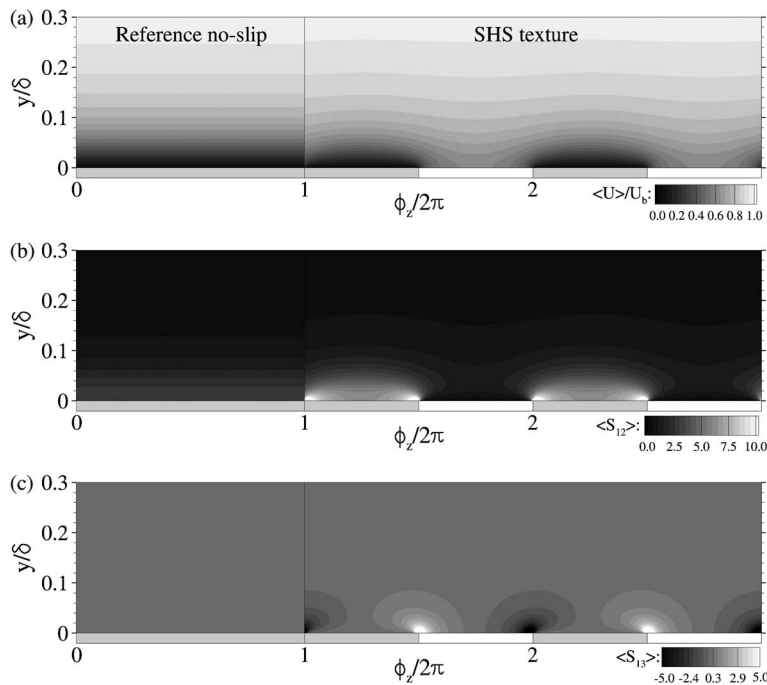


FIG. 10. Phase-averaged primary flow quantities on the transverse ϕ_z - y plane. (a) Streamwise velocity normalized by the bulk value, U_b ; (b) $\langle S_{12} \rangle$ and (c) $\langle S_{13} \rangle$ components of mean rate of strain tensor. Data for both the reference no-slip channel flow ($0 < \phi_z/2\pi < 1$) and the SHS case ($1 < \phi_z/2\pi < 3$) are included for comparison.

contour levels are consistent with the notion of streamwise momentum surplus (deficit) occurring in the free-slip (no-slip) phases (see also Figure 9(b)). Very close to the wall, the corrugated behavior of $\langle u \rangle$ is accentuated significantly and strong spanwise shear is visible in the primary flow. The components of the mean rate of strain tensor,

$$\langle S_{ij} \rangle = \frac{1}{2} \left[\frac{\partial \langle u_i \rangle}{\partial x_j} + \frac{\partial \langle u_j \rangle}{\partial x_i} \right], \quad (14)$$

were evaluated, and contours of $\langle S_{12} \rangle$ and $\langle S_{13} \rangle$ are shown in Figures 10(b) and 10(c), respectively. The highest levels of primary wall-normal shear can be found towards the edges of the no-slip micro-ridges which is consistent with increased levels of skin friction at those locations (see Figure 7). At $y/\delta \approx 0.1875$, $\langle S_{12} \rangle$ exhibits a weak phase-dependence which vanishes above this height. The primary spanwise shear is zero everywhere except at the edges of the free-slip bands and is anti-symmetric about their centers. The regions of high positive (negative) spanwise shear protrude over the edges of the surface texture onto the neighboring no-slip surfaces and, as a result, can possibly influence the levels of skin friction in those regions.

B. Secondary flow

Section III A demonstrated that significant spanwise variations in the primary flow occur in the vicinity of the SHS texture. In turbulent flows, these gradients can result in additional steady fluid motions, or a secondary flow. In general, secondary flows can be classified into two categories, namely, Prandtl's secondary flows of the first and second kind. The former arises due to mean-flow skewing, whereas the latter type is due to anisotropies in the near-wall turbulence. In the current configuration, there is no mechanism to skew the mean shear in the primary flow and, hence, attention is directed to the second type. The analysis is aided by considering vorticity along the primary flow direction,

$$\underbrace{\tilde{v} \frac{\partial \tilde{\Omega}_x}{\partial y} + \tilde{w} \frac{\partial \tilde{\Omega}_x}{\partial z}}_{\text{Convection}} = \underbrace{\frac{1}{Re_b} \nabla^2 \tilde{\Omega}_x}_{\text{Diffusion}} + \underbrace{\left(\frac{\partial^2}{\partial z^2} - \frac{\partial^2}{\partial y^2} \right) \langle R_{23} \rangle}_{P_1} + \underbrace{\frac{\partial^2}{\partial y \partial z} (\langle R_{22} \rangle - \langle R_{33} \rangle)}_{P_2}, \quad (15)$$

where $\tilde{\Omega}_x \equiv \partial \tilde{w} / \partial y - \partial \tilde{v} / \partial z$ is the streamwise vorticity due to the periodic flow. The terms P_1 and P_2 are potential sources of $\tilde{\Omega}_x$ due to Reynolds stress anisotropies.³⁴ Secondary flows of the second kind have been studied in the vicinity streamwise-aligned riblet geometries^{29,35} and in corners of square ducts^{36,37} but are yet to be examined above SHS textures.

The principal interest here is to explain how the secondary flow contributes to local levels of skin friction and to clarify whether it is advantageous or detrimental with respect to the SHS texture performance. An explanation of the direction of the secondary fluid motion is therefore sought. Following the analysis by Perkins,³⁸ the orientation of the secondary flow can be predicted by considering the sign of the production term P_2 in Eq. (15), which can be determined from the near-wall behavior of the turbulence. Consider the series expansions,

$$v' = a_1 + b_1 y + c_1 y^2 + O(y^3), \quad (16a)$$

$$w' = a_2 + b_2 y + c_2 y^2 + O(y^3), \quad (16b)$$

where the coefficients a_i , b_i , and c_i are zero-mean random variables and statistically independent of x , and t . In order for the expansion to be valid, y must be smaller than the distance to the edges of the texture. The near-wall behavior of the Reynolds stresses can be obtained from Eqs. (16a) and (16b) by substituting the no-slip (Eq. (3)) and free-slip (Eq. (4)) boundary conditions and deriving the phase-averaged products of the series expansions. To leading order, the limiting behavior of the Reynolds stresses at the no-slip phase is

$$\langle R_{22} \rangle^{\text{ns}} = \langle c_1^2 y^4 \rangle^{\text{ns}} + \dots, \quad (17a)$$

$$\langle R_{33} \rangle^{\text{ns}} = \langle b_2^2 y^2 \rangle^{\text{ns}} + \dots, \quad (17b)$$

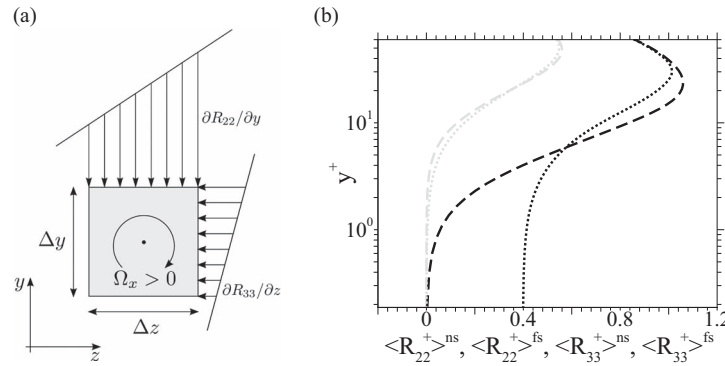


FIG. 11. Mechanism of vorticity production by Reynolds stress anisotropies. (a) Schematic of production mechanism adapted from Perkins;³⁸ (b) profiles of $\langle R_{22}^+ \rangle^{\text{ns}}$ (—), $\langle R_{22}^+ \rangle^{\text{fs}}$ (⋯⋯), $\langle R_{33}^+ \rangle^{\text{ns}}$ (---), and $\langle R_{33}^+ \rangle^{\text{fs}}$ (-⋯-). Reynolds stresses are normalized by $u_{\tau,0}^2$.

and at the free-slip phase,

$$\langle R_{22} \rangle^{\text{fs}} = \langle b_1^2 y^2 \rangle^{\text{fs}} + \dots, \quad (18a)$$

$$\langle R_{33} \rangle^{\text{fs}} = \langle a_2^2 \rangle^{\text{fs}} + \dots. \quad (18b)$$

Profiles of phase-averaged Reynolds stresses from the DNS are shown in Figure 11(b) and demonstrate that $\langle R_{22} \rangle$ has a weak phase dependence since v satisfies the no-penetration condition on all phases. On the other hand, $\langle R_{33} \rangle$ exhibits substantial dependence on the spanwise phase. The sign of P_2 can be determined from the above limiting behavior of turbulent stresses and ignoring $\partial \langle R_{22} \rangle / \partial z$,

$$P_2 \approx -\frac{\partial}{\partial z} \frac{\partial \langle R_{33} \rangle}{\partial y}. \quad (19)$$

Immediately above the free-slip phases, to leading order $\partial \langle R_{33} \rangle^{\text{fs}} / \partial y$ vanishes. Above the no-slip phases, to leading order $\partial \langle R_{33} \rangle^{\text{ns}} / \partial y = 2 \langle b_2^2 y \rangle^{\text{ns}} + \dots$. Therefore, the spanwise derivative of $\partial \langle R_{33} \rangle / \partial y$ is positive (P_2 is negative) when we traverse from the free-slip to the no-slip region. As a result, the vorticity in this region is counterclockwise, $\tilde{\Omega}_x < 0$. An opposite vorticity is established, $\tilde{\Omega}_x > 0$, when we traverse from the no-slip to the free-slip region. In this case, the spanwise derivative of $\partial \langle R_{33} \rangle / \partial y$ is negative and therefore P_2 is positive. The present analysis therefore predicts that the secondary currents should exhibit a counter-rotating pattern.

Vectors of $(\langle v \rangle, \langle w \rangle) = (\tilde{v}, \tilde{w})$ are shown in Figure 12 superimposed on contours of streamwise vorticity $\tilde{\Omega}_x$. The vectors show the pairs of counter-rotating streamwise vortices, whose rotation agrees with the preceding analysis. The cores of the secondary vortices are positioned at $y^+ \approx 13$ and have a core-to-core spacing of $\Delta z^+ \approx 34$, a distance that is approximately equal to the spanwise spacing of the surface features. Note that in a laminar flow simulation, no secondary motions

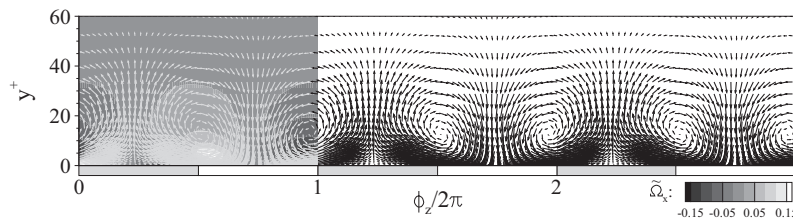


FIG. 12. Phase-averaged secondary flow in the cross-flow plane, ϕ_z - y . Contours indicate streamwise vorticity, $\tilde{\Omega}_x$ ($0 < \phi_z/2\pi < 1$), and vectors are in-plane velocities, (\tilde{v}, \tilde{w}) . For clarity, only every second vector in the wall-normal direction and every third vector in the spanwise direction are plotted.

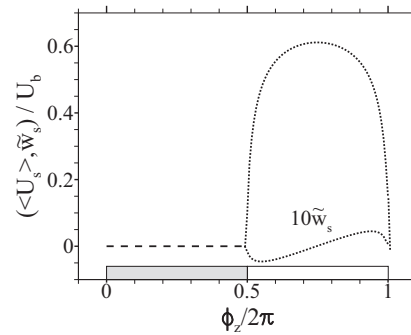


FIG. 13. Slip velocity profiles normalized by the bulk velocity, U_b . Both the streamwise, $\langle u_s \rangle$, and spanwise, \tilde{w}_s , slip velocity profiles are plotted across no-slip (---) and free-slip (····) phases. Note that the spanwise slip velocity profile has been multiplied by a factor of 10.

emerge above the SHS texture since turbulence is a prerequisite for Prandtl's secondary flow of the second kind. A comparable scenario is encountered for streamwise-aligned riblet geometries where a secondary flow can be supported in a fully developed turbulent flow,²⁹ but cannot be sustained over the same geometry in a laminar flow.³⁹

Over the free-slip region, the secondary flow resembles an impinging jet (Figure 12). Near the surface, the flow crosses onto the no-slip region and a growing boundary layer forms on the wall as the central no-slip phase is approached. Above the central no-slip region, the flow resembles opposing jets which lead to an upwash. The maximum wall-normal and spanwise secondary velocities are 0.5% and 0.9% of the bulk value, respectively.

In terms of skin friction, the lateral wall-jet at the edges of the no-slip band can lead to a performance penalty, since mean streamwise momentum will be convected from the fast moving free-slip region to the no-slip edges of the micro-ridges. On the other hand, the steady upwash of momentum away from the wall can yield a performance gain by reducing the near-wall shear.

C. Slip flow

Significant effort has been devoted to quantify the average streamwise slip velocity, $\langle U_s \rangle^{xz}$, for turbulent flow over textured surfaces both in experiments⁸ and simulations.^{22,23} On the other hand, the role of a spanwise slip velocity has not been examined in the context of the current surface model. It has, however, been credited for increasing the level of turbulent skin friction in the case of the Navier slip model.^{11,13,15}

Both streamwise and spanwise slip velocity profiles are shown in Figure 13. The maximum streamwise slip velocity is $\langle U_s \rangle / U_b = 0.62$ and occurs at the central free-slip phase. The average slip velocity across all phases is $\langle U_s \rangle^{xz} / U_b = 0.27$. A maximum spanwise slip velocity $\tilde{w} / U_b = \pm 0.0085$ is achieved near the edge of the interface. At the edges of the free-slip region, the spanwise slip velocity advects momentum outwards towards the edges of the no-slip region, which is consistent with the orientation of the secondary vortices shown in Figure 12. The spanwise slip velocity profile is antisymmetric about the central free-slip phase and integrates to zero when averaged across all phases.

Previous DNS studies have delineated the effect of streamwise and spanwise slip velocities on SHS texture performance, where either isotropic^{11,15} or anisotropic¹³ effective slip-lengths were prescribed using the Navier slip model only. In general, streamwise slip was found to reduce skin-friction drag, whereas spanwise slip increased drag. The latter effect is due to the spanwise slip strengthening near-wall streamwise vortices.

In order to examine the effects of streamwise and spanwise slip on skin friction for the current SHS texture, two additional numerical experiments were conducted: the spanwise (streamwise) slip was eliminated by replacing the free-slip boundary condition on spanwise (streamwise) velocity with a no-slip boundary condition. In the first case with exclusive streamwise slip, the skin-friction

coefficient was reduced relative to the original SHS texture. For the case with exclusive spanwise slip, the skin friction exceeded the value from the reference channel flow. These results are therefore consistent with earlier studies¹¹ where exclusive streamwise (spanwise) slip was found to have a beneficial (detrimental) influence on drag.

IV. TURBULENCE STATISTICS

This section details changes in the turbulence statistics in the presence of the SHS texture. Relative to the reference no-slip channel flow, Sec. III demonstrated that the mean fluid motions above the SHS texture are markedly different, characterized by spanwise variations in the primary flow (Figure 10), counter-rotating secondary streamwise vortices in the cross-flow plane (Figure 12), and slipping fluid motions on the texture itself (Figure 13). The focus here is to evaluate the statistical changes in perturbation fields and to identify how these changes may influence the local levels of skin friction.

A. Turbulence kinetic energy

Contours of the phase-averaged turbulence kinetic energy, $\langle k \rangle \equiv \frac{1}{2} \langle R_{ii} \rangle$, are shown in Figure 14. Relative to the reference no-slip channel flow, the TKE distribution above the SHS texture shows three main differences. First, a suppression of TKE across all phases is apparent for $y^+ > 20$. Second, spanwise variations occur in the buffer region ($10 < y^+ < 20$), where the strongest (weakest) TKE is found above the central no-slip (free-slip) phases. Finally, in the region very close to the SHS texture ($0 < y^+ < 10$), while TKE above no-slip phases naturally tends to zero, it persists all the way to the surface of the free-slip phases.

The evolution of TKE is governed by

$$\frac{\partial \langle k \rangle}{\partial t} + \langle u_j \rangle \frac{\partial \langle k \rangle}{\partial x_j} = \langle P \rangle + \langle \Pi \rangle + \langle D \rangle + \langle \epsilon \rangle + \langle T \rangle, \quad (20)$$

where

$$\langle P \rangle = -\langle R_{ij} \rangle \langle S_{ij} \rangle, \quad (21a)$$

$$\langle \Pi \rangle = -\left\langle u'_i \frac{\partial p'}{\partial x_i} \right\rangle, \quad (21b)$$

$$\langle D \rangle = \frac{1}{Re_b} \frac{\partial^2 \langle k \rangle}{\partial x_j \partial x_j}, \quad (21c)$$

$$\langle \epsilon \rangle = -\frac{1}{Re_b} \left\langle \left(\frac{\partial u'_i}{\partial x_j} \right)^2 \right\rangle, \quad (21d)$$

$$\langle T \rangle = -\frac{\partial}{\partial x_j} \langle k u'_j \rangle. \quad (21e)$$

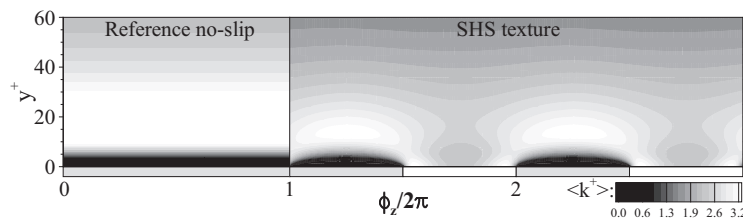


FIG. 14. Phase-averaged turbulence kinetic energy in the cross-flow ϕ_z - y plane for the reference no-slip channel flow ($0 < \phi_z/2\pi < 1$) and the SHS case ($1 < \phi_z/2\pi < 3$).

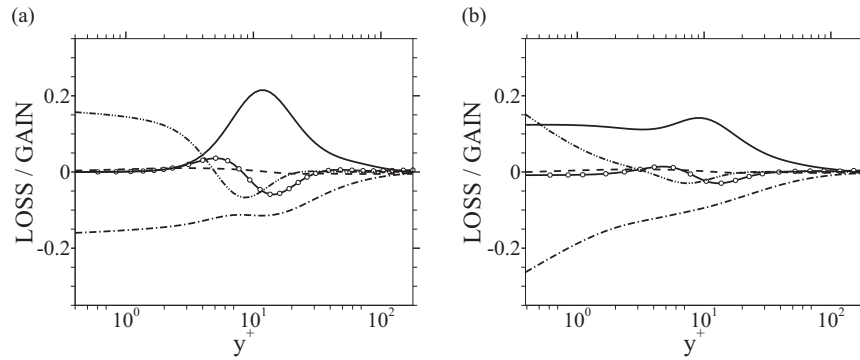


FIG. 15. TKE budget averaged across all phases for (a) the reference no-slip channel flow and (b) the SHS case. Production $\langle P \rangle^{xz}$ (—); dissipation $\langle \epsilon \rangle^{xz}$ (- - -); redistribution $\langle \Pi \rangle^{xz}$ (- · - ·); turbulent transport $\langle T \rangle^{xz}$ (- · -); and viscous diffusion $\langle D \rangle^{xz}$ (- · · -). All terms are normalized by $u_{\tau,0}^4 Re_b$.

Terms in the TKE budget averaged across all phases are reported in Figure 15. Relative to the reference no-slip channel flow, peak production is reduced by approximately 34% and its wall-normal height decreases by approximately 25%. Also note that the production of TKE persists all the way to the wall.

In Figure 16(a), the budget terms are shown when averaged across the no-slip phases only. Relative to the reference channel flow, the peak value of production is reduced by 10%, and its wall-normal location is shifted closer to the wall. This shift causes an increase in production at $y^+ \simeq 5$. The dissipation, on the other hand, is enhanced at all wall-normal positions. The balance is maintained in the region $y^+ \simeq 5$ by the local increase in production, $\langle P \rangle^{ns}$, and by the increase in the turbulent transport, $\langle T \rangle^{ns}$. Nearer to the wall, the balance is maintained by viscous diffusion,

$$\langle D \rangle^{ns} = \underbrace{\frac{1}{Re_b} \frac{\partial^2 \langle k \rangle^{ns}}{\partial y^2}}_{\langle D_y \rangle^{ns}} + \underbrace{\frac{1}{Re_b} \frac{\partial^2 \langle k \rangle^{ns}}{\partial z^2}}_{\langle D_z \rangle^{ns}}, \quad (22)$$

while advection by the secondary flow,

$$\langle C \rangle^{ns} = \underbrace{\left\langle \tilde{v} \frac{\partial \langle k \rangle}{\partial y} \right\rangle^{ns}}_{\langle C_y \rangle^{ns}} + \underbrace{\left\langle \tilde{w} \frac{\partial \langle k \rangle}{\partial z} \right\rangle^{ns}}_{\langle C_z \rangle^{ns}}, \quad (23)$$

remains insignificant (see Figure 16(b)).

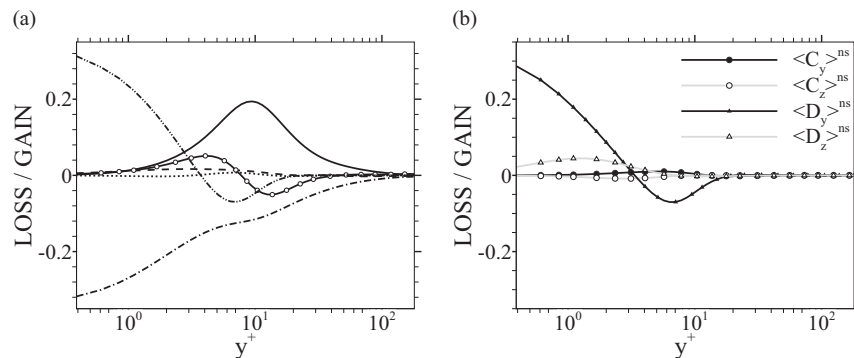


FIG. 16. (a) TKE budget averaged across all no-slip phases for the SHS case. Production $\langle P \rangle^{ns}$ (—); dissipation $\langle \epsilon \rangle^{ns}$ (- - -); redistribution $\langle \Pi \rangle^{ns}$ (- · - ·); turbulent transport $\langle T \rangle^{ns}$ (- · -); viscous diffusion $\langle D \rangle^{ns}$ (- · · -); and advection by the secondary flow $\langle C \rangle^{ns}$ (· · · ·). (b) Line profiles of viscous transport (Eq. (22)) and advection by the secondary flow (Eq. (23)). All terms are normalized by $u_{\tau,0}^4 Re_b$.

The suppression of peak production, $\langle P \rangle^{xz}$, was observed in the laboratory experiments by Woolford *et al.*⁹ However, due to experimental restrictions, their nearest measurement location to the wall was $y^+ \approx 7-10$. The spanwise variation of the near-wall TKE reported here (see Figure 14), and in particular its increase near the no-slip/free-slip interface, motivates a more detailed examination of the production term.

The total TKE production is decomposed into,

$$\langle P \rangle = \overbrace{\langle P_I \rangle + \langle P_{II} \rangle}^{\text{Primary production}} + \underbrace{\tilde{P}_I + \tilde{P}_{II} + \tilde{P}_{III}}_{\text{Secondary production}}, \quad (24)$$

where

$$\langle P_I \rangle = -\langle R_{12} \rangle \frac{\partial \langle u \rangle}{\partial y}, \quad (25a)$$

$$\langle P_{II} \rangle = -\langle R_{13} \rangle \frac{\partial \langle u \rangle}{\partial z}, \quad (25b)$$

$$\tilde{P}_I = -\langle R_{22} \rangle \frac{\partial \tilde{v}}{\partial y}, \quad (25c)$$

$$\tilde{P}_{II} = -\langle R_{23} \rangle \left(\frac{\partial \tilde{v}}{\partial z} + \frac{\partial \tilde{w}}{\partial y} \right), \quad (25d)$$

$$\tilde{P}_{III} = -\langle R_{33} \rangle \frac{\partial \tilde{w}}{\partial z}. \quad (25e)$$

Therefore, both the primary and secondary fluid motions contribute to TKE production. The respective root-mean-squared values of all five terms were evaluated across all phases, and the first two, namely, $\langle P_I \rangle$ and $\langle P_{II} \rangle$, were found to be most dominant.

Contours of total TKE production are shown in Figure 17(a). Relative to the reference no-slip channel flow, TKE production is weakened above the no-slip phases and enhanced at the edges of the interface. Contours of $\langle P_I \rangle$ are shown in Figure 17(b). This term is reduced across all phases in the region $5 < y^+ < 20$, and is weakest above the free-slip phases. The averaged behavior of $\langle P_I \rangle$ across all phases agrees qualitatively with the reduction in $\langle P \rangle^{xz}$ in Figure 15. For $y^+ < 5$, small pockets of negative $\langle P_I \rangle$ are visible close the edges of the SHS features. Energy is therefore transferred from the stochastic fluctuations to the mean flow in that region. Considering that $\langle S_{12} \rangle > 0$ for all y (see Figure 10(b)), the negative $\langle P_I \rangle$ is due to the sign of the Reynolds shear stress, $\langle R_{12} \rangle$, which is discussed in Sec. IV B. TKE production due to $\langle P_{II} \rangle$, which is only relevant to the SHS configuration, is shown in Figure 17(b). Above the SHS texture, localized lobes of intense production originate at the edges of the free-slip interface, protrude outwards and arch over the edges of neighboring no-slip micro-features. The spanwise shear in the primary flow (see Figure 10(c)) permits the production of TKE at this interface, and corresponds well with the regions of increased TKE shown in Figure 14.

B. Turbulent shear stresses

The mean streamwise momentum equation is given by

$$\tilde{v} \frac{\partial \langle u \rangle}{\partial y} + \tilde{w} \frac{\partial \langle u \rangle}{\partial z} = -\frac{d \langle p \rangle}{dx} + \frac{1}{Re_b} \left(\frac{\partial^2 \langle u \rangle}{\partial y^2} + \frac{\partial^2 \langle u \rangle}{\partial z^2} \right) - \left(\frac{\partial \langle R_{12} \rangle}{\partial y} + \frac{\partial \langle R_{13} \rangle}{\partial z} \right). \quad (26)$$

The last two terms on the right-hand side are the influence of the Reynolds stresses on the mean flow. Therefore, any changes to the stresses or additional terms that arise due to the SHS texture can modify the velocity profile and, in turn, skin friction. In the case of reference no-slip channel flow,

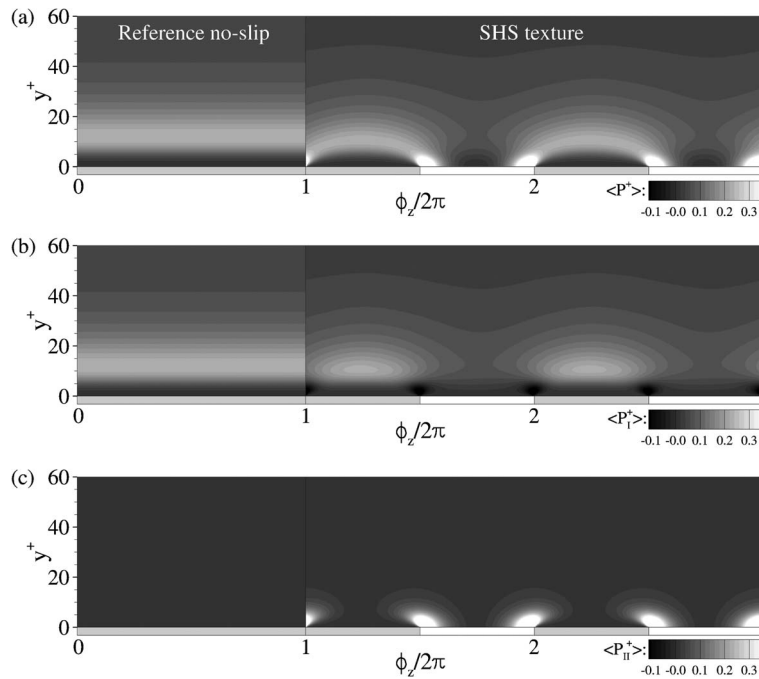


FIG. 17. Phase-averaged TKE production in the cross-flow ϕ_z - y plane for reference no-slip channel flow ($0 < \phi_z/2\pi < 1$) and the SHS case ($1 < \phi_z/2\pi < 3$). (a) $\langle P^+ \rangle$; (b) $\langle P_1^+ \rangle$; (c) $\langle P_{II}^+ \rangle$. All terms are normalized by $u_{\tau,0}^4 Re_b$.

the term $\partial \langle R_{12} \rangle / \partial y$ redistributes the mean momentum: it retards the flow in the core of the channel and accelerates it near the wall. Relative to a parabolic laminar profile, this trend increases the skin friction. The term $\partial \langle R_{13} \rangle / \partial z$ on the other hand only arises in the SHS case. This subsection examines the changes to $\langle R_{12} \rangle$ and the additional Reynolds stresses supported by the presence of SHS texture and their propensity to distort the mean flow.

Contours of $\langle R_{12} \rangle$ are shown in Figure 18(a). For $y^+ > 15$, the Reynolds shear stress is suppressed across all phases above the SHS texture. Below $y^+ \approx 5$, small pockets of $\langle R_{12} \rangle > 0$ occur close to where the edges of the interface and micro-feature meet, and coincide with the regions of negative TKE production shown previously in Figure 17(a). Contours of $\langle R_{13} \rangle$ are shown in Figure 18(b). Above the SHS texture, the distribution of $\langle R_{13} \rangle$ is antisymmetric about the central no-slip and free-slip phases. The contours resemble protruding lobes that originate at the edges of the interface, which arch out over the neighboring micro-features. They are similar in shape to the contours of TKE production reported in Figure 17(b). The net lateral force due to the action of $\partial \langle R_{13} \rangle / \partial z$ can be expressed as

$$\begin{aligned} \mathbf{F}_z &= \frac{1}{L_x d} \int_0^{L_x} \int_0^1 \int_0^d \frac{\partial \langle R_{13} \rangle}{\partial z} dz dy dx \\ &= \frac{1}{L_x d} \int_0^{L_x} \int_0^1 [\langle R_{13} \rangle]_0^d dy dx. \end{aligned} \quad (27)$$

Therefore, the net contribution of $\partial \langle R_{13} \rangle / \partial z$ is due to the values at the edges at the SHS texture. Due to the anti-symmetry of $\langle R_{13} \rangle$ the force is additive and $\mathbf{F}_z \neq 0$. At present, however, it remains unclear if this lateral force contributes towards the local levels of skin friction in a favorable or adverse manner.

Contours of $\langle R_{23} \rangle$ are shown in Figure 18(c). This term only occurs above the SHS texture. Although it does not appear on the right-hand side of the mean streamwise momentum equation

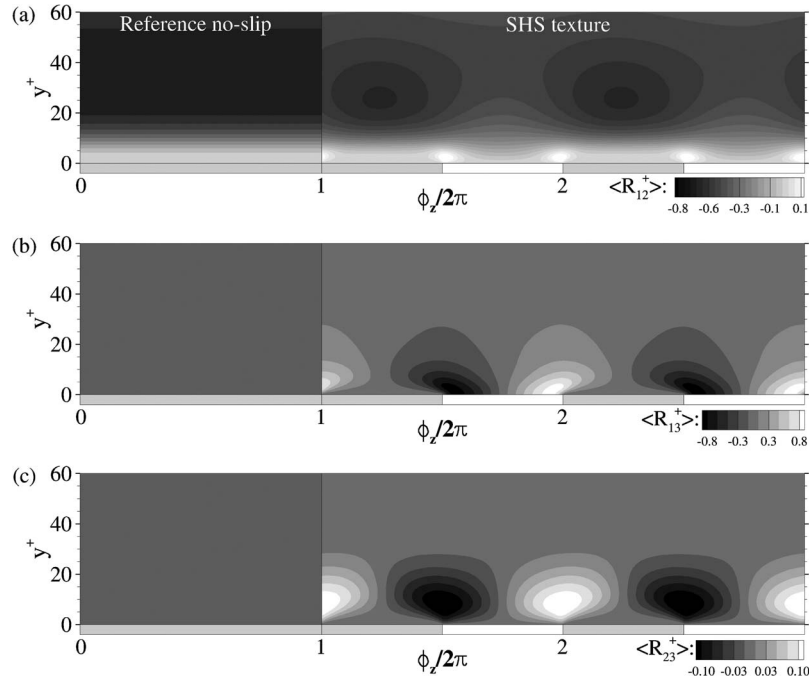


FIG. 18. Reynolds shear stresses in the cross-flow ϕ_z - y plane for the reference no-slip channel flow ($0 < \phi_z/2\pi < 1$) and SHS case ($1 < \phi_z/2\pi < 3$). (a) $\langle R_{12}^+ \rangle$; (b) $\langle R_{13}^+ \rangle$; and (c) $\langle R_{23}^+ \rangle$. All terms are normalized by $u_{\tau,0}^2$.

(Eq. (26)), it is helpful in explaining the origin, or production, of the localized patches of positive Reynolds shear stress shown in Figure 18(a). The Reynolds stress production tensor is given by

$$\langle P_{ij} \rangle = -\langle R_{ik} \rangle \frac{\partial \langle u_j \rangle}{\partial x_k} - \langle R_{jk} \rangle \frac{\partial \langle u_i \rangle}{\partial x_k}. \quad (28)$$

Therefore,

$$\langle P_{12} \rangle = \overbrace{\langle P_{12,I} \rangle + \langle P_{12,II} \rangle}^{\text{Primary shear production}} + \underbrace{\tilde{P}_{12,I} + \tilde{P}_{12,II}}_{\text{Secondary shear production}}, \quad (29)$$

where

$$\langle P_{12,I} \rangle = -\langle R_{22} \rangle \frac{\partial \langle u \rangle}{\partial y}, \quad (30a)$$

$$\langle P_{12,II} \rangle = -\langle R_{23} \rangle \frac{\partial \langle u \rangle}{\partial z}, \quad (30b)$$

$$\tilde{P}_{12,I} = -\langle R_{12} \rangle \frac{\partial \tilde{v}}{\partial y}, \quad (30c)$$

$$\tilde{P}_{12,II} = -\langle R_{13} \rangle \frac{\partial \tilde{v}}{\partial z}, \quad (30d)$$

which shows that both primary and secondary flow gradients contribute towards the production of $\langle R_{12} \rangle$. The first two terms which correspond to primary-flow contributions are dominant. Figure 19 compares contours of the production of Reynolds shear stress (Eq. (29)), including $\langle P_{12,I} \rangle$ for the reference channel flow and $\langle P_{12,I} \rangle$ and $\langle P_{12,II} \rangle$ for the SHS case. The term $\langle P_{12,I} \rangle$ is always negative since both $\langle R_{22} \rangle$ and $\partial \langle u \rangle / \partial y$ are positive. Contours of $\langle P_{12,II} \rangle$, on the other hand, have a positive

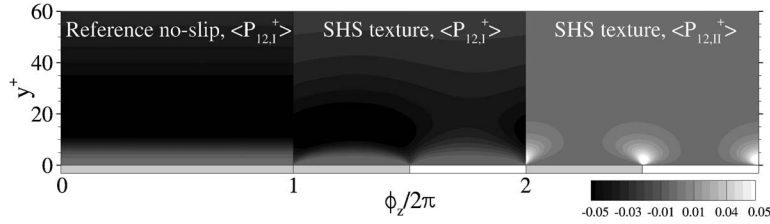


FIG. 19. Production of Reynolds shear stress in the cross-flow ϕ_z - y plane for reference no-slip channel flow ($0 < \phi_z/2\pi < 1$) and SHS case ($1 < \phi_z/2\pi < 3$). All terms are normalized by $u_{\tau,0}^4 Re_b$.

sign which leads to the regions of positive $\langle R_{12} \rangle$ in Figure 18(a), and the corresponding negative contribution to TKE production $\langle P_I \rangle$ in Figure 17(b).

V. SKIN-FRICTION IDENTITY

In this section, we quantify the contributions of primary, secondary, and stochastic fluid motions to the local levels of skin friction (see Figure 7). These contributions are analyzed using a modification of the identity by Fukagata *et al.*⁴⁰ hereafter referred to as FIK. The FIK identity is derived by taking the triple integral of the streamwise component of the RANS equation (26) in the wall-normal direction. Here, the FIK identity is derived in phase-averaged form and, after some manipulation, can be written as

$$\begin{aligned}
 \langle C_f \rangle_{\text{FIK}} = & \underbrace{\frac{6}{\langle U_b \rangle Re_b} \left(1 - \frac{\langle U_s \rangle}{\langle U_b \rangle} \right)}_{\text{Laminar contribution, } \langle C_f \rangle_{\text{lam}}} + \underbrace{\frac{6}{\langle U_b^2 \rangle} \int_0^1 (1-y) \langle -R_{12} \rangle dy}_{\text{ } \langle R_{12} \rangle \text{ contribution, } \langle C_f \rangle_{R_{12}}} \\
 & - \underbrace{\frac{3}{\langle U_b^2 \rangle} \int_0^1 (1-y)^2 \left(\overline{\tilde{v} \frac{\partial \langle u \rangle}{\partial y}} \right) dy}_{\text{Wall-normal advection, } \langle C_f \rangle_{\tilde{v}}} - \underbrace{\frac{3}{\langle U_b^2 \rangle} \int_0^1 (1-y)^2 \left(\overline{\tilde{w} \frac{\partial \langle u \rangle}{\partial z}} \right) dy}_{\text{Spanwise advection, } \langle C_f \rangle_{\tilde{w}}} \\
 & + \underbrace{\frac{3}{\langle U_b^2 \rangle} \int_0^1 (1-y)^2 \left(-\frac{\partial \langle R_{13} \rangle}{\partial z} \right) dy}_{\text{ } \langle R_{13} \rangle \text{ contribution, } \langle C_f \rangle_{R_{13}}} + \underbrace{\frac{3}{\langle U_b^2 \rangle Re_b} \int_0^1 (1-y)^2 \frac{\partial^2 \langle \overline{u} \rangle}{\partial z^2} dy}_{\text{Spanwise diffusion, } \langle C_f \rangle_{\text{zdiff}}}, \quad (31)
 \end{aligned}$$

where $\overline{\langle \cdot \rangle} = \langle \cdot \rangle - \int_0^1 \langle \cdot \rangle dy$ denotes how a phase-averaged variable varies relative to its local bulk mean value. The six terms on the right-hand side of the phase-averaged FIK identity have the following interpretation: The first term, $\langle C_f \rangle_{\text{lam}}$, is identical to the laminar solution plus the effect of the streamwise slip velocity. The second term, $\langle C_f \rangle_{R_{12}}$, is the contribution by the Reynolds shear stress. The third and fourth terms, $\langle C_f \rangle_{\tilde{v}}$ and $\langle C_f \rangle_{\tilde{w}}$, are the wall-normal and spanwise convection of the primary flow by the secondary flow. The fifth term, $\langle C_f \rangle_{R_{13}}$, is the contribution made by the spanwise gradient of $\langle R_{13} \rangle$. The final term, $\langle C_f \rangle_{\text{zdiff}}$, is the spanwise diffusion of the primary streamwise momentum. Note that $\langle C_f \rangle$ is zero over free-slip phases, and $\langle U_s \rangle = 0$ over no-slip phases. The above expression is, however, general and can be subsequently averaged across no-slip, free-slip or all phases. The various contributions to $\langle C_f \rangle$ were not explained by Martell *et al.*^{22,23} Instead that work only reported that $\langle C_f \rangle^{\text{xz}}$ is reduced due to the average streamwise slip velocity.

In order to verify the accuracy of the phase-averaged FIK identity, $\langle C_f \rangle_{\text{FIK}}$ from Eq. (31) was compared to $\langle C_f \rangle$ evaluated directly from the mean velocity profile. Figure 20 shows the close agreement between $\langle C_f \rangle_{\text{FIK}}$ and $\langle C_f \rangle$ at all spanwise phases. Averaged across all phases, the

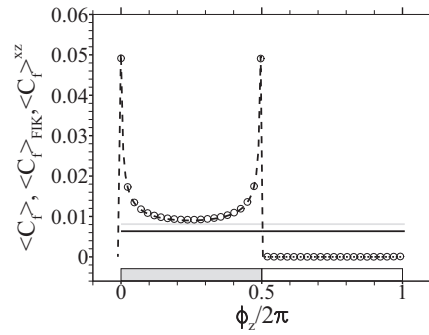


FIG. 20. Phase-averaged skin-friction coefficients computed directly from $\langle C_f \rangle$ (---) and from the FIK identity $\langle C_f \rangle_{\text{FIK}}$ (○). The skin-friction coefficient averaged across all phases, $\langle C_f \rangle^{xz}$, is included for both the reference no-slip channel flow (—) and the SHS case (—).

skin-friction coefficients corresponding to the FIK identity, $\langle C_f \rangle_{\text{FIK}}^{xz}$, and the direct value, $\langle C_f \rangle^{xz}$, agree to within 1%.

Each term in the phase-averaged FIK identity (Eq. (31)) was evaluated and subsequently integrated across all no-slip phases to obtain the various contributions to $\langle C_f \rangle_{\text{FIK}}^{\text{ns}}$. A breakdown of $\langle C_f \rangle_{\text{FIK}}^{\text{ns}}$ is shown in Figure 21, where data for the reference no-slip channel flow and SHS are included for comparison. Also shown are the results for laminar flow over the SHS texture. Terms with a positive sign are performance penalties and negative terms are performance gains.

The primary flow makes two contributions to skin friction: the laminar term, $\langle C_f \rangle_{\text{lam}}^{\text{ns}}$, and the spanwise diffusion term, $\langle C_f \rangle_{\text{zdiff}}^{\text{ns}}$. The former can be interpreted as the reference skin friction with the rest of the terms in the FIK identity providing the change due to flow configuration. The $\langle C_f \rangle_{\text{zdiff}}^{\text{ns}}$ term represents a performance penalty incurred due to the spanwise diffusion of high-momentum fluid above the free-slip band onto no-slip regions. The secondary flow makes two contributions to skin friction for the textured case through the terms $\langle C_f \rangle_{\tilde{v}}^{\text{ns}}$ and $\langle C_f \rangle_{\tilde{w}}^{\text{ns}}$. The former is the only negative contribution towards skin friction and represents the steady wall-normal advection of streamwise momentum away from the no-slip wall by the secondary motion. The term $\langle C_f \rangle_{\tilde{w}}^{\text{ns}}$ represents a performance penalty due to the spanwise advection of streamwise momentum towards the edges of the no-slip bands. The signs of both these terms agree with the orientation of the secondary flow shown in Figure 12. The stochastic fluid motions also make two contributions to skin friction through the terms $\langle C_f \rangle_{R12}^{\text{ns}}$ and $\langle C_f \rangle_{R13}^{\text{ns}}$. Relative to the reference channel flow, the performance penalty due to $\langle C_f \rangle_{R12}^{\text{ns}}$ is reduced by 20% for the textured case. The term $\langle C_f \rangle_{R13}^{\text{ns}}$ is also a performance penalty due to lateral turbulent momentum transfer (Eq. (27)). It is clear that from Figure 21 and Table III that the terms $\langle C_f \rangle_{R12}^{\text{ns}}$ and $\langle C_f \rangle_{R13}^{\text{ns}}$ make the largest contribution to skin friction and, in fact, account

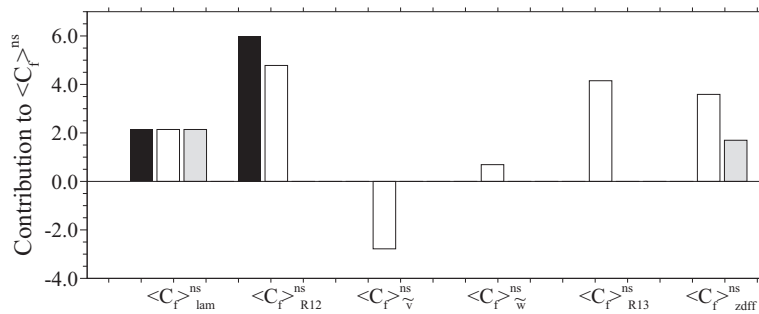


FIG. 21. Contributions of terms in the FIK identity (Eq. (31)) towards the skin-friction coefficient averaged across all no-slip phases, $\langle C_f \rangle_{\text{FIK}}^{\text{ns}}$. Reference no-slip channel flow (■); streamwise-aligned texture with turbulent (□); and laminar (▒) flow conditions. All terms have been multiplied by a factor of 10^3 .

TABLE III. Contributions of terms in the FIK identity (Eq. (31)) to the skin-friction coefficient averaged across all no-slip phases, $\langle C_f \rangle_{\text{FIK}}^{\text{ns}}$. All terms have been multiplied by a factor of 10^3 .

Case	$\langle C_f \rangle_{\text{lam}}^{\text{ns}}$	$\langle C_f \rangle_{R_{12}}^{\text{ns}}$	$\langle C_f \rangle_{\bar{v}}^{\text{ns}}$	$\langle C_f \rangle_{\bar{w}}^{\text{ns}}$	$\langle C_f \rangle_{R_{13}}^{\text{ns}}$	$\langle C_f \rangle_{\text{zdiff}}^{\text{ns}}$	$\langle C_f \rangle_{\text{FIK}}^{\text{ns}}$
Reference	2.142	5.976	0.000	0.000	0.000	0.000	8.118
SHS texture	2.142	4.783	-2.781	0.691	4.153	3.589	12.577
Reference (laminar)	2.142	0.000	0.000	0.000	0.000	0.000	2.142
SHS texture (laminar)	2.142	0.000	0.000	0.000	0.000	1.697	3.839

for approximately 71% of the total value of $\langle C_f \rangle_{\text{FIK}}^{\text{ns}}$. This observation motivates a closer inspection of the Reynolds shear stresses in the vicinity of the SHS texture.

VI. TURBULENCE STRUCTURES

In Sec. V it was shown that the Reynolds shear stresses, $\langle R_{12} \rangle$ and $\langle R_{13} \rangle$, contribute significantly to the skin friction. In this section, we report quadrant analysis of both terms. The results are complemented by a study of instantaneous vortical structures.

A. Quadrant analysis

Quadrant analysis classifies the contributions of various flow events to $\langle R_{ij} \rangle$ by dividing the Reynolds shear stresses into four quadrants according to the signs of the stochastic fluid motions.^{41,42} Quadrants two and four (Q2 and Q4) events contribute towards a negative Reynolds shear stress ($\langle R_{ij} \rangle < 0$). Quadrants one and three (Q1 and Q3) events contribute towards a positive Reynolds shear stress ($\langle R_{ij} \rangle > 0$). In the present flow, the analysis is performed for both $\langle R_{12} \rangle$ and $\langle R_{13} \rangle$ which exchange mean momentum in the y - and z -directions, respectively. In analogy to the Q2 (low-speed ejection) and Q4 (high-speed sweep) events that produce $\langle R_{12} \rangle = \langle u'v' \rangle$, similar events can be defined for $\langle R_{13} \rangle = \langle u'w' \rangle$. In this case, Q2 (Q4) events can be interpreted as the positive (negative) lateral displacement of low-speed (high-speed) fluid.

The contribution of each quadrant to the Reynolds shear stress averaged across the no-slip phases, $\langle R_{12} \rangle^{\text{ns}}$, is shown in Figure 22(a). Relative to the reference channel flow, the peak activity in Q2 and Q4 is suppressed by 23% and 17%, respectively, in response to the presence of the SHS texture. Furthermore, the wall-normal positions of peak Q2 and Q4 events move closer to the wall. This downward shift of ejections and sweeps agrees well with previous studies which suggest that turbulent structures remain intact and are simply shifted towards the SHS texture.²² However, Martell *et al.*²² did not differentiate between no-slip and free-slip regions since they averaged their results across all phases. The activity in the first and third quadrants is suppressed with the exception of a notable bulge in Q1 in the region $y/\delta < 0.1$. The enhanced near-wall activity in the first quadrant is representative of the regions of positive Reynolds shear stress (Figure 18) and the associated negative TKE production. In summary, relative to the reference channel flow, the SHS texture is effective at suppressing both sweep and ejection events, and hence influences the ejection and sweep motions in a favorable manner for the purpose of drag reduction. Simultaneously, the texture also effects a local beneficial change in the background turbulence manifest as Q1 activity. Relative to the reference channel flow, the averaged effect across all four quadrants yields a reduction of turbulence production as shown in Figure 17(a), and corroborates the weaker contribution of the Reynolds shear stress to skin friction shown in Figure 21.

The quadrant analysis of $\langle R_{13} \rangle$ is shown in Figure 22(b). Due to its form in the momentum equation (26) and in the FIK identity (31), the analysis of $\langle R_{13} \rangle$ is reported at three spanwise phases, $\phi_z = \{\pi/2, 3\pi/4, \pi\}$, in order to emphasize its spanwise variation. The results demonstrate that the turbulence activity intensifies in Q2 and Q4 as the edge of the micro-feature is approached ($\phi_z \rightarrow \pi$), while it weakens in Q1 and Q3. Averaged across all four quadrants (see inset in Figure 22(b)), the combined effect of Q2 and Q4 events outweighs that of Q1 and Q3. The negative spanwise gradient

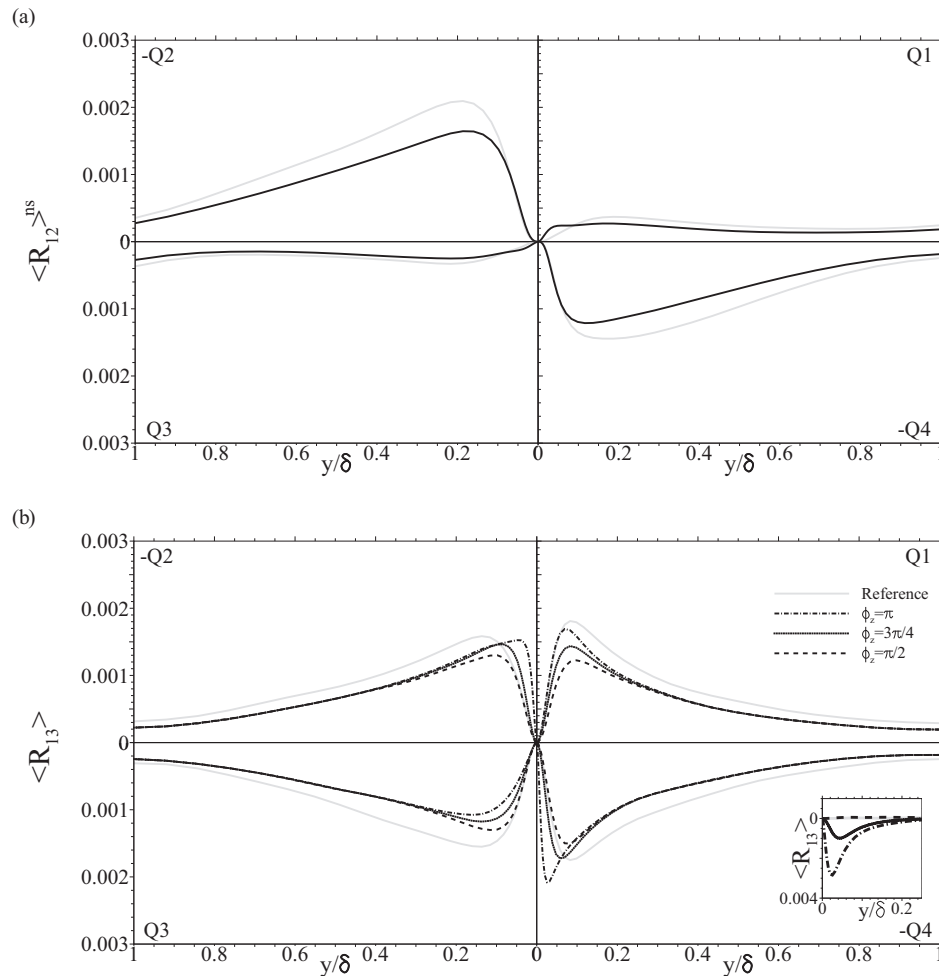


FIG. 22. Quadrant analysis of (a) Reynolds shear stress averaged across all no-slip phases, $\langle R_{12} \rangle^{ns}$, for the reference channel flow (—) and SHS (---); (b) phase-averaged $\langle R_{13} \rangle$ at spanwise phases $\phi_z = \{\pi/2, 3\pi/4, \pi\}$. Profiles are normalized by U_b^2 .

of $\langle R_{13} \rangle$ results in a significant positive contribution to the levels of skin friction as was shown in Figure 21. In analogy to the sweeps and ejections in the y -direction, Q2 and Q4 events that create $\langle R_{13} \rangle$ correspond to the lateral displacements of low- and high-speed streamwise momentum, respectively. A physical interpretation of a Q4 event in Figure 22(b), for example, is the lateral translation of high-speed fluid from the free-slip region onto the edges of the no-slip band by negative spanwise perturbations. The high intensity of Q4 events at no-slip phases, therefore, should decrease as the central no-slip phase is approached—a trend which is clearly visible in Figure 22(b).

B. Vortical structures

Vortical structures are closely related to the production of Reynolds shear stress.⁴³ An analysis of vortical structures is performed in order to examine the organized motions of turbulence that manifest themselves as the statistical trends conveyed in the turbulence shear stresses and quadrant analyses which, ultimately, contribute towards the levels of skin friction.

The λ_2 criterion proposed by Jeong and Hussain⁴⁴ is employed to detect vortical structures in the instantaneous stochastic perturbation field. Examples of the three-dimensional structures are visualized in Figure 23. Relative to the reference channel flow, there is an appreciable decrease in the population of vortex cores above the SHS texture. Instantaneous realizations such as Figure 23

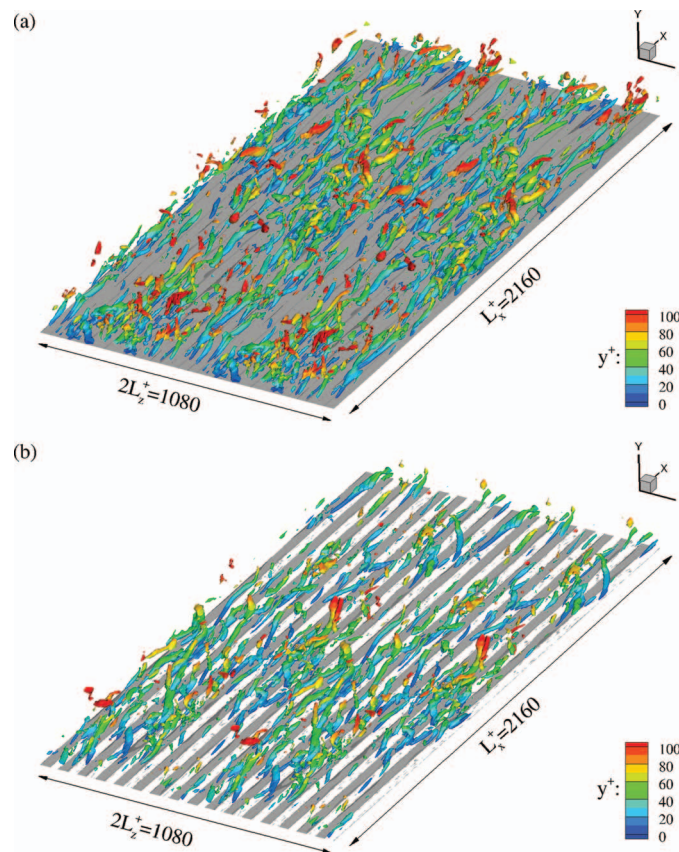


FIG. 23. Isosurfaces of vortical structures using $\lambda_2 / (u_{\tau,0}^4 Re_b^2) = -0.01$. (a) Reference channel flow; (b) SHS case. Color indicates the wall-normal location of the isosurface. Note that the domain has been repeated in the spanwise direction.

provide empirical evidence that turbulence activity is reduced in response to the presence of the SHS texture. Further corroboratory evidence is, however, desirable.

Statistics of λ_2 were computed from 250 instantaneous three-dimensional fields, separated by 30 wall time-units each. The probability density functions (PDF) of $0.002 \leq -\lambda_2 / (u_{\tau,0}^4 Re_b^2) \leq 0.04$ at $y^+ = 18$ and $y^+ = 50$ are shown in Figure 24. In the presence of the SHS texture, there is a clear reduction in the PDF for $-\lambda_2 / (u_{\tau,0}^4 Re_b^2) > 0.01$ at both wall-normal positions. The results indicate that vortical activity is suppressed both in the buffer layer (Figure 24(a)) and above (Figure 24(b)). These statistics support the observations from the instantaneous fields (e.g., Figure 23). Weakened vortices have been reported in various drag-reduced flows where both active³⁰ and passive⁴⁵ flow control approaches have been employed. The less frequent occurrence of vortices at both wall-normal positions was manifested as decreased Q2 and Q4 events at the same locations in the quadrant analysis (Figure 22(a)).

To statistically characterize the vortical structures further, an eduction algorithm was developed in order to investigate their spatial orientation and population density. The methodology is adapted from previous work on detection of streaks in transitional flows.^{46,47} The three basic steps of the eduction algorithm are: (i) identify vortex cores at a given level of $\lambda_2 / (u_{\tau,0}^4 Re_b^2)$; (ii) discard vortical structures whose streamwise length satisfies $\Delta x^+ < 150$; (iii) store the local coordinates of individual vortical structures. Unless otherwise stated, statistics presented herein are computed using $\lambda_2 / (u_{\tau,0}^4 Re_b^2) = -0.01$.

Using the local coordinates of each vortex core, the pitch angle, α , and the yaw angle, Ψ , were computed, and PDFs of both quantities were evaluated over the range $10 < y^+ < 180$. The PDF of the pitch angle is shown in Figure 25(a) for both the reference channel flow and the textured

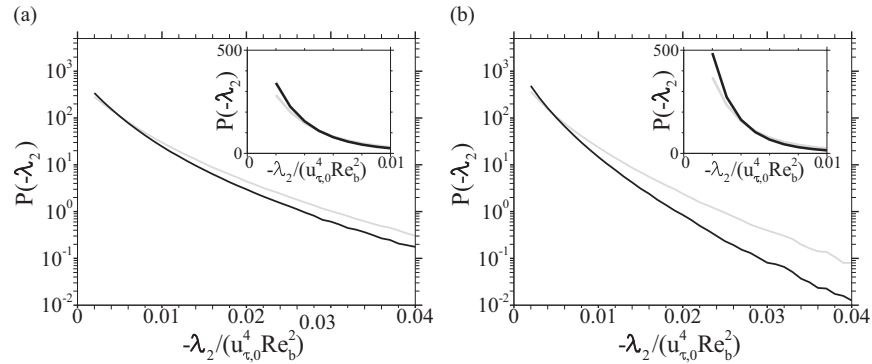


FIG. 24. PDFs of $-\lambda_2 / (u_{\tau,0}^4 Re_b^2)$ at (a) $y^+ = 18$ and (b) $y^+ = 50$ including data for both the reference channel flow (—) and the SHS (—).

configuration. No significant differences between the two PDFs are observed. Vortex cores are most likely to be positively inclined at $\alpha = 6^\circ$ and the mean pitch angle is $\alpha = 9^\circ$, which is in agreement with the values reported by Jeong *et al.*⁴⁸ The PDF of the yaw angle, Ψ , is shown in Figure 25(b) and indicates that vortex cores are most likely to be aligned along the primary flow direction, corresponding to $\Psi = 0^\circ$, for both the reference channel flow and the SHS configuration.

In general, the PDFs of α and Ψ reflect the orientation of the instantaneous vortical structures shown in Figure 23. The PDFs (Figure 25) suggest that, relative to the reference channel flow, the presence of the SHS texture and the associated secondary flow do not drastically alter the orientation of the vortical structures. This result can be contrasted to other flow control strategies, for example, the pronounced harmonic yawing of near-wall streaks due to spanwise wall oscillations⁴⁹ or the reduced inclination of vortical structures in response to wall-heating.⁴⁵

The population density of vortex cores, or the number of vortex cores per unit volume, was evaluated from the 250 snapshots and is denoted ρ_{λ_2} . The vortex identification was performed with a threshold $0.003 \leq -\lambda_2 / (u_{\tau,0}^4 Re_b^2) \leq 0.03$ across the interval $10 < y^+ < 180$, and the results are shown in Figure 26. Relative to the reference channel flow, ρ_{λ_2} is reduced for all values of λ_2 , which indicates that the populations of both weak and strong vortical motions are reduced due to the presence of the SHS texture. As remarked by Robinson,⁴³ vortical structures with any orientation other than wall normal have the ability to act as “pumps” that induce sweeps and ejections, which contribute to the Reynolds shear stress, $\langle R_{12} \rangle$. As a consequence of their reduced population density (Figure 26) and strength (Figure 24), the net pumping of the vortex cores is suppressed and this is manifest as reductions in Q2 and Q4 activity (Figure 22(a)) which, ultimately, reduces the Reynolds shear stress contribution to skin friction. However, this effect is overshadowed by a significant

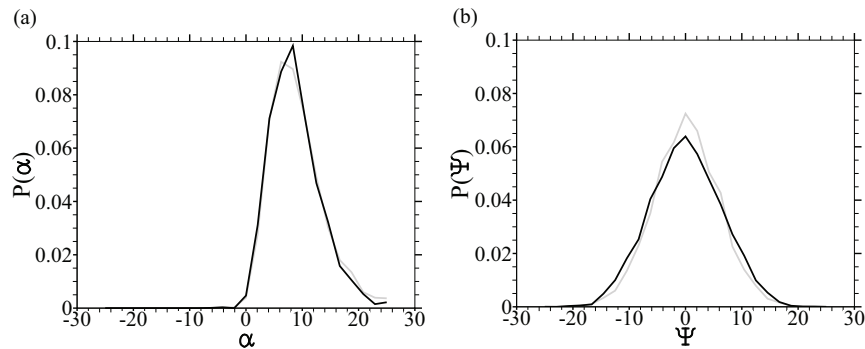


FIG. 25. PDFs of (a) pitch angle, α , and (b) yaw angle, Ψ , including data for both the reference channel flow (—) and the SHS case (—). Each PDF is evaluated across the wall-normal interval $10 < y^+ < 180$.

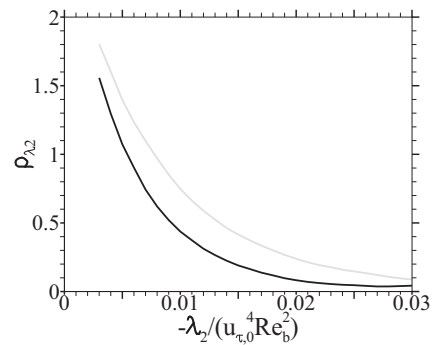


FIG. 26. Population density of vortex cores, ρ_{λ_2} , as a function of $-\lambda_2 / (u_{\tau,0}^4 Re_b^2)$. Reference channel flow (—); SHS case (—).

increase in $\langle R_{13} \rangle$ which limits the drag-reducing capacity of the surface texture directly through $\langle C_f \rangle_{R_{13}}$, and indirectly via $\langle C_f \rangle_{z\text{diff}}$.

VII. SUMMARY AND CONCLUSIONS

DNS of turbulent flow in a channel with superhydrophobic surfaces were performed at a fixed bulk Reynolds number, $Re_b = 2800$. Both channel walls were modeled as textured streamwise-aligned micro-ridges using alternating no-slip and free-slip boundary conditions. A reference simulation with regular no-slip walls was also performed at $Re_\tau = 180$ for comparison. Relative to the reference flow, the SHS texture reduced the mean skin-friction coefficient by 21.6%. A detailed analysis of changes to the base flow, turbulence kinetic energy budget, and the near-wall vortical structures was performed.

Previous studies of turbulent channel flow over SHS textures^{22–24} have reported statistical quantities averaged in both the streamwise and spanwise directions, and attributed drag reduction to the mean streamwise slip velocity. In the present work, we examined the phase-averaged statistics and focused on the no-slip region. In addition, the generation of a periodic secondary flow of Prandtl's second kind and its proclivity to influence the levels of skin friction were demonstrated. The phase-averaged TKE budget was also evaluated, and the influence of the SHS texture on the terms in the budget was assessed. The statistical response of the turbulent fluid motions was further explained using quadrant analyses and an examination of turbulence structures.

A discussion is presented of the increased skin friction on the SHS features. In analogy to the reference channel flow where the wall-normal gradient of the Reynolds shear stress redistributes the mean velocity profile in a manner that increases skin friction, the mean flow above the SHS features is subject to additional (i) primary, (ii) secondary flow, and (iii) turbulence effects: (i) The high-speed streamwise momentum above the free-slip regions diffuses in the spanwise direction onto low-speed regions and contributes to the increased levels of skin friction, $\langle C_f \rangle_{z\text{diff}}$. (ii) The secondary flow has a dual effect. The spanwise component displaces high momentum from the free-slip onto the no-slip zone thus increasing drag, $\langle C_f \rangle_{\bar{w}}$. The wall-normal component, on the other hand, forces an upwash above the no-slip region thus reducing drag, $\langle C_f \rangle_{\bar{v}}$. The latter effect is more dominant and, therefore, the secondary flow has an overall favorable impact on drag reduction. (iii) The terms of the TKE budget averaged across all no-slip phases demonstrated that the production term is weakened in the buffer layer while dissipation is enhanced at the wall. The former observation was corroborated using quadrant analysis of the Reynolds shear stress averaged across all no-slip phases, $\langle R_{12} \rangle^{\text{ns}}$. The quadrant analysis demonstrated that both ejection and sweep events are suppressed by the presence of the SHS. Analysis of $\langle R_{13} \rangle$ demonstrated that this component wields a significant contribution towards skin friction, $\langle C_f \rangle_{R_{13}}$. This term also indirectly contributes to $\langle C_f \rangle_{z\text{diff}}$ due to its influence on the $\langle U \rangle^{\text{ns}}$ profile.

The current results provide a detailed account of the changes to the TKE budget and the factors that contribute to enhanced drag on the no-slip phases for a SHS texture with $g^+ = d^+ = 33.75$ (normalized using reference values from a conventional channel flow at $Re_\tau = 180$). The performance penalties and gains due to the primary, secondary, and stochastic fluid motions were delineated and their contribution to the levels of skin friction across the SHS texture was quantified. Recently, Park *et al.*²⁴ reported that drag reduction is enhanced as the texture spacing is increased to $g^+ = d^+ = 100$. Their work provided integral performance measures, and analysis similar to that presented herein can be adopted to examine the origin of the performance gains. Future work should also investigate the effects of spatially varying SHS textures⁵⁰ and of more realistic surface models which resolve, for example, the deformable gas-liquid interface.⁵¹

- ¹ W. Barthlott and C. Neinhuis, "Purity of the sacred lotus, or escape from contamination in biological surfaces," *Planta* **202**, 1–8 (1997).
- ² K. Watanabe, Y. Udagawa, and H. Udagawa, "Drag reduction of Newtonian fluid in a circular pipe with a highly water-repellent wall," *J. Fluid Mech.* **381**, 225–238 (1999).
- ³ J. Ou, B. Perot, and J. P. Rothstein, "Laminar drag reduction in microchannels using ultrahydrophobic surfaces," *Phys. Fluids* **16**, 4635–4643 (2004).
- ⁴ A. Cassie and S. Baxter, "Wettability of porous surfaces," *Trans. Faraday Soc.* **40**, 546–551 (1944).
- ⁵ R. Wenzel, "Resistance of solid surfaces to wetting by water," *Ind. Eng. Chem.* **29**, 988–994 (1936).
- ⁶ J. Ou and J. P. Rothstein, "Direct velocity measurements of the flow past drag-reducing ultrahydrophobic surfaces," *Phys. Fluids* **17**, 103606 (2005).
- ⁷ J. Ou, G. R. Moss, and J. P. Rothstein, "Enhanced mixing in laminar flows using ultrahydrophobic surfaces," *Phys. Rev. E* **76**, 016304 (2007).
- ⁸ R. J. Daniello, N. E. Waterhouse, and J. P. Rothstein, "Drag reduction in turbulent flows over superhydrophobic surfaces," *Phys. Fluids* **21**, 085103 (2009).
- ⁹ B. Woolford, J. Prince, D. Maynes, and B. W. Webb, "Particle image velocimetry characterization of turbulent channel flow with rib patterned superhydrophobic walls," *Phys. Fluids* **21**, 085106 (2009).
- ¹⁰ C. Navier, "Memoire sur les lois du mouvement des fluides," *Mem. Acad. R. Sci. Inst. France* **6**, 389–416 (1823).
- ¹¹ T. Min and J. Kim, "Effect of hydrophobic surface on skin-friction drag," *Phys. Fluids* **7**, 55–58 (2004).
- ¹² T. Min and J. Kim, "Effect of hydrophobic surface on stability and transition," *Phys. Fluids* **17**, 108106 (2005).
- ¹³ A. Busse and N. D. Sandham, "Influence of an anisotropic slip-length boundary condition on turbulent channel flow," *Phys. Fluids* **24**, 055111 (2012).
- ¹⁴ D. You and P. Moin, "Effects of hydrophobic surfaces on the drag and lift of a circular cylinder," *Phys. Fluids* **19**, 081701 (2007).
- ¹⁵ K. Fukagata, N. Kasagi, and P. Koumoustaskos, "A theoretical prediction of friction drag reduction in turbulent flow by superhydrophobic surfaces," *Phys. Fluids* **18**, 051703 (2006).
- ¹⁶ J. R. Philip, "Flows satisfying mixed no-slip and no-shear conditions," *J. Appl. Math. Phys.* **23**, 353–372 (1972).
- ¹⁷ J. R. Philip, "Integral properties of flows satisfying mixed no-slip and no-shear conditions," *J. Appl. Math. Phys.* **23**, 960–968 (1972).
- ¹⁸ E. Lauga and H. Stone, "Effective slip in pressure-driven stokes flow," *J. Fluid Mech.* **489**, 55–77 (2003).
- ¹⁹ A. M. J. Davis and E. Lauga, "Hydrodynamic friction of fakir-like superhydrophobic surfaces," *J. Fluid Mech.* **661**, 402–411 (2010).
- ²⁰ C. Ybert, C. Barentin, C. Cottin-Bizonne, P. Joseph, and L. Bocquet, "Achieving large slip with superhydrophobic surfaces: Scaling laws for generic geometries," *Phys. Fluids* **19**, 123601 (2007).
- ²¹ Y. P. Cheng, C. J. Teo, and B. C. Khoo, "Microchannel flows with superhydrophobic surfaces: Effects of Reynolds number and pattern width to channel height ratio," *Phys. Fluids* **21**, 122004 (2009).
- ²² M. B. Martell, J. B. Perot, and J. P. Rothstein, "Direct numerical simulations of turbulent flows over superhydrophobic surfaces," *J. Fluid Mech.* **620**, 31–41 (2009).
- ²³ M. B. Martell, J. B. Perot, and J. P. Rothstein, "An analysis of superhydrophobic turbulent drag reduction mechanisms using direct numerical simulation," *Phys. Fluids* **22**, 065102 (2010).
- ²⁴ H. Park, H. Park, and J. Kim, "A numerical study of the effects of superhydrophobic surface on the skin-friction drag in turbulent channel flow," *Phys. Fluids* **25**, 110815 (2013).
- ²⁵ M. Rosenfeld, D. Kwak, and M. Vinokur, "A fractional step solution method for the unsteady incompressible Navier–Stokes equations in generalized coordinate systems," *J. Comput. Phys.* **94**, 102–137 (1991).
- ²⁶ A. K. M. F. Hussain and W. C. Reynolds, "The mechanisms of an organized wave in turbulent shear flow," *J. Fluid Mech.* **31**, 241–258 (1970).
- ²⁷ J. Kim, P. Moin, and R. Moser, "Turbulence statistics in fully developed channel flow at low Reynolds number," *J. Fluid Mech.* **177**, 133–166 (1987).
- ²⁸ W. J. Jung, N. Mangiavaachi, and R. Akhavan, "Suppression of turbulence in wall-bounded flows by high-frequency spanwise oscillations," *Phys. Fluids* **4**, 1605–1607 (1992).
- ²⁹ H. Choi, P. Moin, and J. Kim, "Direct numerical simulations of turbulent flow over riblets," *J. Fluid Mech.* **255**, 503–539 (1993).
- ³⁰ H. Choi, P. Moin, and J. Kim, "Active turbulence control for drag reduction in wall-bounded flows," *J. Fluid Mech.* **262**, 75–110 (1994).

- ³¹ B. E. Launder and S. Li, "A numerical study of riblet effects on laminar flow through a plane channel," *Appl. Sci. Res* **46**, 271 (1989).
- ³² J. L. Lumley, "Drag reduction in turbulent flow by polymer additives," *J. Polymer Sci. D: Macromol. Rev.* **7**, 263 (1973).
- ³³ M. J. Walsh, "Turbulent boundary layer drag reduction using riblets," AIAA Paper No. 82-0169, 1982.
- ³⁴ P. Bradshaw, "Turbulent secondary flows," *Annu. Rev. Fluid Mech.* **19**, 53–74 (1987).
- ³⁵ D. Goldstein and T. C. Tuan, "Secondary flow induced by riblets," *J. Fluid Mech.* **363**, 115–151 (1998).
- ³⁶ F. B. Gessner, "The origin of secondary flow in turbulent flow along a corner," *J. Fluid Mech.* **58**, 1–25 (1973).
- ³⁷ A. Huser and S. Biringen, "Direct numerical simulations of turbulent flow in a square duct," *J. Fluid Mech.* **257**, 65–95 (1993).
- ³⁸ H. J. Perkins, "The formation of streamwise vorticity in turbulent flow," *J. Fluid Mech.* **44**, 721–740 (1970).
- ³⁹ H. Choi, P. Moin, and J. Kim, "On the effect of riblets in fully developed laminar channel flows," *Phys. Fluids* **3**, 1892 (1991).
- ⁴⁰ K. Fukagata, K. Iwamoto, and N. Kasagi, "Contribution of Reynolds stress distribution to the skin friction in wall-bounded flows," *Phys. Fluids* **14**, 73–76 (2002).
- ⁴¹ W. W. Willmarth and S. S. Lu, "Structure of the Reynolds stress near the wall," *J. Fluid Mech.* **55**, 65 (1972).
- ⁴² J. M. Wallace, H. Eckelmann, and R. S. Brodkey, "The wall region in turbulent shear flow," *J. Fluid Mech.* **54**, 39 (1972).
- ⁴³ S. K. Robinson, "Coherent motions in the turbulent boundary layer," *Annu. Rev. Fluid Mech.* **23**, 601–39 (1991).
- ⁴⁴ J. Jeong and F. Hussain, "On the identification of a vortex," *J. Fluid Mech.* **285**, 69–94 (1995).
- ⁴⁵ J. Lee, S. Y. Jung, H. J. Sung, and T. A. Zaki, "Effect of wall heating on turbulent boundary layers with temperature-dependent viscosity," *J. Fluid Mech.* **726**, 196–225 (2013).
- ⁴⁶ K. P. Nolan and T. A. Zaki, "Conditional sampling of transitional boundary layers in pressure gradients," *J. Fluid Mech.* **728**, 306–339 (2013).
- ⁴⁷ T. A. Zaki, "From streaks to spots and onto turbulence: Exploring the dynamics of boundary layer transition," *Flow. Turbul. Combust.* **91**, 451–473 (2013).
- ⁴⁸ J. Jeong, F. Hussain, W. Schoppa, and J. Kim, "Coherent structures near the wall in a turbulent channel flow," *J. Fluid Mech.* **332**, 185 (1997).
- ⁴⁹ E. Toubert and M. A. Leschziner, "Near-wall streak modification by spanwise oscillatory wall motion and drag-reduction mechanisms," *J. Fluid Mech.* **693**, 150–200 (2011).
- ⁵⁰ Y. Hasegawa, B. Frohnafel, and N. Kasagi, "Effects of spatially varying slip length on friction drag reduction in wall turbulence," *J. Phys.: Conf. Ser.* **318**, 022028 (2011).
- ⁵¹ M. Sbragaglia and A. Prosperetti, "A note on the effective slip properties for microchannel flows with ultrahydrophobic surfaces," *Phys. Fluids* **19**, 043603 (2007).